# Fiber Optic Sensor for In-Situ State-of-Charge Monitoring for Lithium-Ion Batteries

by

Liliana Zdravkova

A thesis
presented to the University of Waterloo
in fulfillment of the
thesis requirement for the degree of
Master of Applied Science
in
Mechanical Engineering

Waterloo, Ontario, Canada, 2014

# AUTHOR'S DECLARATION

I hereby declare that I am the sole author of this thesis. This is a true copy of the thesis, including any required final revisions, as accepted by my examiners.

I understand that my thesis may be made electronically available to the public.

# Abstract

The objective of this thesis is to develop a fiber optic sensor for in-situ measurement of the optical properties of Li-ion batteries for the purpose of state-of-charge (SOC) estimation. Current methods rely on measuring the external parameters of the battery, namely voltage, current and temperature, and using various algorithms to estimate the SOC of the battery. These methods vary in accuracy and cost; generally, there is a trade-off between the two. A direct measurement of the internal state of the battery has to this point not been demonstrated as a means of SOC estimation in full cell Li-ion batteries. This could be a way to obtain more accurate estimates at a lower cost.

The electrodes of Li-ion batteries have been found to exhibit changing optical characteristics at different states of charge. This is especially apparent in the graphite electrode, which visibly changes in colour. Spectroscopy studies of electrodes extracted from batteries charged to different SOC values have confirmed the visual observations and have also shown changes at non-visible wavelengths. In order to measure optical changes in a live cycling battery a sensor must be incorporated into the cell. Silica fibers lend themselves to this application as they are non-reactive to the electrolyte in the battery and they can be used to make evanescent wave sensors. The evanescent wave sensor consists of a fiber with partially removed cladding that is placed in contact with the anode such that the evanescent fields interact with the electrode. The measured signal is based on the intensity modulation of the light carried by the fiber, which allows for a low cost system to be used to detect the sensor output.

A method was developed to insert the sensor in a working full cell battery prepared in a Swagelok® cell. Several tests were carried out and the sensor signal recorded as the cell was charged and discharged. The signal follows the charging and discharging of the battery consistently for both full and partial cycles and the sensor response is repeatable with different sensors and battery cells. The sensor response has three regions, with the central region, between 30-60% SOC, having very high sensitivity. The optical signal can be used to estimate the SOC with an accuracy of 14% or better. The accuracy can be greatly improved with more stable batteries and an improved signal acquisition system.

The sensor response was compared to an analytical model of evanescent wave sensors. The transfer matrix method is used for the model as it provides an elegant way of modeling reflection and transmission through multi layers of optical media, such as the three layer stack formed by the core and cladding of the

sensor and the battery electrode. The model may be used to relate the optical properties of the electrodes to the SOC of the battery.

In summary, a fiber optic evanescent wave sensor has been developed that can be used to estimate the SOC of Li-ion batteries. The sensor is novel as it measures the internal state of the battery directly and can be used to obtain estimates in real time. A simple, low-cost system is used for acquiring the sensor signal. The sensor has high sensitivity and good accuracy in estimating the SOC.

## Acknowledgements

I would like to thank my supervisor Patricia Nieva for her support and guidance throughout my degree. I would also like to thank my colleagues Ryan Norris, Krishna Iyer, Jeremy Godin, AbdulRahman Ghannoum and Victor Chabot for their insight and suggestions. I am grateful to my family for backing me up and allowing me to take the time to complete this degree.

# Table of Contents

# List of Figures

# List of Tables

# Chapter 1
# Introduction

Lithium-ion batteries have become very common as energy storage devices due to their capacity for high energy density. They are used for a multitude of applications, including electronic devices and electric vehicles. An important aspect of any energy storage system is knowledge of the amount of stored energy that is still available. In batteries this is known as state of charge (SOC). The SOC is defined as the amount of charge left as a ratio of the maximum charge that the battery can hold. Most devices that use Li-ion batteries have some manner of displaying the SOC, with some being more accurate than others.

Fiber optic sensors are used widely for many different applications. They are ideal for use in industrial environments as they are immune to the electromagnetic interference present in these settings. They can also be used for remote sensing as the fiber provides a channel with very low signal loss. Fiber optics can be made from materials, such as glass, that are resistant to chemicals and to high temperatures, and can be used in harsh environments. Their small form factor also allows them to be used in tight spaces. These properties make fiber optic sensors a candidate for monitoring the internal state of batteries.

## 1.1 Motivation

Knowledge of the SOC is important for all battery systems, and in particular for electric vehicle applications. In electric vehicles it is important that the batteries do not run out of charge unexpectedly and leave the vehicle stranded. Li-ion batteries are also susceptible to damage due to over- or under-charging, which decreases the lifetime of the battery. For this reason wide safety margins are built into the battery management systems of electric vehicles. The batteries are not cycled over their full SOC range and thus the full capacity of the battery is not utilized. If the SOC estimate was more precise and reliable it would be possible to increase the usable range of the battery without risking damage. This would allow for more efficient sizing and use of the batteries.

Current SOC estimation methods for Li-ion batteries rely on measurements of the external parameters of the battery, including voltage, current and temperature. Several methods have been developed for

estimating the SOC based on these parameters and high accuracy has been demonstrated in laboratory environments. There is difficulty in transferring these methods to the field and practical applications due to greater uncertainties in the environment. Some methods also require bulky and costly measurement and signal processing equipment, which cannot be incorporated into portable systems or systems where weight is a limitation and cost margins are tight, such as electric vehicles.

## 1.2 Thesis Objectives

This thesis presents the development of an optical sensor intended for in-situ SOC measurement and estimation in Li-ion batteries. The sensor measures the internal battery chemistry directly and provides an indication of the battery status in real time. The most important characteristic of the sensor is that it provides a useful output that reflects the current state of the battery. An equally important aspect is that the battery remains functional at all times and does not lose performance with the incorporated sensor. Electric vehicle battery packs can contain hundreds or thousands of battery cells, which means that cost is also an important factor for any battery management system. The sensor presented here is specifically designed to meet the following objectives:

- Accurate measurements of the SOC in real time.
- No interference with the performance of the battery.
- Ability to withstand the chemical environment inside the battery and continue functioning for the life of the battery.
- Low cost per sensor.

## 1.3 Thesis Organization

This thesis is divided into seven chapters. Chapter 2 presents a literature review on SOC estimation methods, Li-ion battery properties and optical sensors. Several methods for estimating SOC are discussed along with the advantages and drawbacks of each. Findings on the optical properties of battery electrodes demonstrate the possibility of using optical sensors to monitor their internal state. The chapter summarizes the various types of fiber optic sensors and their applications, and concludes with the applicability of such sensors to battery electrodes.

In Chapter 3 background information and design considerations for the sensor are presented. The internal environment of the battery presents several challenges that guide the design of the form

factor of the sensor. The choice of optical sensing mechanism is examined in terms of achieving the design objectives. Additionally, design decisions regarding the properties of the sensor, such as operational wavelength and geometric parameters are discussed. The chapter concludes with a summary of the design.

Chapter 4 presents background theory on fiber optic evanescent wave sensors. The conditions for the presence of the evanescent wave are developed, as well as the properties of the wave. These properties are discussed in terms of the behavior of the fiber optic sensor. The transfer matrix method is described and is employed to determine the effects of the optical properties of an external medium applied to the sensor. The transfer matrix method is used as it provides an elegant way of modeling reflection and transmission through multi layers of optical media, such as the three layer stack formed by the sensor and external medium. The applicability of the model to determining a relationship between battery electrode properties and SOC is also discussed.

Chapter 5 details the fabrication of the sensor and its insertion into prototype batteries. The sensor is created by etching optical fibers to reduce the cladding to a specific thickness. The sensor is characterized by measuring the transmission power loss when a high refractive index liquid is applied to the sensing region. The sensor is incorporated into a Li-ion battery assembled in a modified Swagelok® cell. Experiments are presented that show the presence of the sensor does not affect battery performance, and that support the choice of wavelength. Further experimental results show the viability of the in-situ battery sensor setup and the repeatability of the obtained signal.

Chapter 6 details the signal processing used to achieve a useful signal, which includes high frequency and thermal noise compensation, and normalization that allows for comparison of the results from different battery cells. Properties of the sensor, such as sensitivity, accuracy and hysteresis are analyzed. An estimation of SOC based on the measured sensor signals is proposed and discussed. Finally, the experimental results are compared with the model presented in Chapter 4.

The thesis concludes with Chapter 7, which outlines the contributions and conclusions of the thesis and proposes future work to develop the sensor for commercial applications.

# Chapter 2
# Literature Review

This chapter reviews literature relevant to the development of the fiber optic battery sensor, including current methods of SOC estimation, studies on optical properties of graphite electrodes and implementations of optical sensors.

## 2.1 SOC Estimation

SOC estimation has been a challenge since batteries have been relied upon to provide power. With the development of electric and hybrid electric vehicles this has become an even more important topic. Li-ion batteries have pushed this further as the need for SOC estimation for these systems has grown beyond the necessity of knowing how much power is left in the battery. Proper battery management not only makes these batteries more reliable, but can also have a significant impact on the lifetime of the battery.

Most SOC estimation methods measure the external electrical parameters of the battery, namely voltage, current and temperature, and use various techniques to relate these to the SOC. The suitability of each of these methods depends on the application and the requirements for SOC estimation accuracy.

Coulomb counting measures the current going into and out of the battery to keep track of the charge. This is a very simple method and widely used as it is relatively easy to implement [1]. Its accuracy depends mainly on the precision of the current sensors and on the initial SOC estimate. It is susceptible to long term error accumulation, which is mainly caused by two factors. The first is that the charging and discharging process is not 100% efficient and not all the current going into the battery is converted to charge, therefore less charge is available than went into the battery. This is handled to some extent by estimating efficiency losses and incorporating them into the SOC calculation, however, requiring the compensation makes the method more complex, thus reducing one of its main advantages. The second factor is that the overall capacity declines as the battery ages, meaning that the same amount of charge will not translate to the same SOC value. In order to improve the SOC estimation recalibration points can be used to correct the estimate [2]. It is not

always practical to bring the energy storage system to recalibration points and in many cases the system will need to be out of commission for a time while recalibration is performed. These considerations make Coulomb counting infeasible for many applications.

Open Circuit Voltage (OCV) is the voltage achieved when the battery has been disconnected from the circuit and allowed to rest for a period of time until it reaches equilibrium. The OCV can be a good indicator of SOC, however it varies from one battery to the next, even for the same chemistries [3]. Another issue is that it cannot be used for real-time SOC estimation, as it requires a rest period on the order of hours to achieve the OCV. For this reason it is usually used in model-based SOC estimation where the OCV is estimated by the model and then the OCV-SOC relationship is applied to the SOC estimate [4]–[6]. Model-based approaches require the measurement of several parameters, mainly voltage, current and temperature, and sufficient processing capacity to calculate the desired output parameters. This can increase the cost and requires good models to achieve high accuracy.

The SOC can also be estimated from impedance measurements [7], [8]. An AC signal, current or voltage, is applied to the battery and the impedance is calculated from the resulting current and voltage. An equivalent circuit model is then used to relate the impedance to SOC. Impedance measurements can be done at a single frequency, which is simple but does not yield as much information, or for a spectrum of frequencies, which gives insight into many different parameters that affect the SOC and SOH. The former is relatively simple to implement, but only gives a high-level picture of the battery behavior. The latter provides insight into many different parameters that affect the SOC and SOH, but is difficult to implement in practice as it has quite intensive data analysis requirements. Impedance measurements are generally difficult to reproduce as temperature and other factors can influence the measurement and yield better results when combined with other methods [9], [10]. The complexity of the equipment necessary to perform accurate impedance-based SOC estimation makes this method impractical for many applications, such as electric vehicles.

Another method for SOC estimation is based on Kalman filtering [11]–[13]. A Kalman Filter (KF) is a method of modeling a dynamic system using a set of recursive equations. In batteries this approach uses current and voltage measurements to predict the SOC based on previously accumulated data and the current measurement. The main sources of error are the nonlinearities in the battery system and inaccuracies in the model. Due to nonlinearities inherent in battery systems the extended or unscented

KF is usually used, both of which can model nonlinear systems. Improved battery models increase the accuracy of this method [14], and adaptive KF algorithms can also compensate for errors [15]. Using KF is a popular method, especially for electric vehicles, as it allows for real-time dynamic SOC estimation. The drawback is that it is computationally intensive and requires measurement of several parameters, leaving room for improvement if sensor and processing requirements can be reduced.

Computational logic, such as Artificial Neural Networks (ANN) and Fuzzy Logic has also been applied to SOC estimation [16]–[18]. These methods use a set of data to train an algorithm to predict the SOC. They can be used independently or combined with KF methods [19]. For ANN the network can be trained offline or online. The former method requires significant computation time for training offline prior to being applied to a battery in the field, but is subsequently more prone to errors if the battery differs from the data used in training. To overcome this problem an adaptive neural network can be used [20], however it requires online collection of data and training, which increases the computational load during operation, which results in the same issues as KF.

Each of the methods mentioned above has advantages and drawbacks and, in general, increased accuracy comes at an increased cost, either in precise sensors or computational capacity or both. These methods have in common that they rely on external measurements of the battery current and voltage, and in some cases temperature. Another approach would be to measure the battery chemistry directly by embedding sensors inside the cell. This has been demonstrated with some types of lead-acid batteries where the electrolyte density is measured and related to SOC [21], [22]. For other types of batteries it is more difficult to integrate a sensor into the cell.

The idea of embedding optical sensors into batteries has been recently proposed in a patent [23] that describes a system where one or more fiber optic based sensors are used to monitor the state of energy storage devices such as batteries. This approach is similar to the sensor presented in this thesis with one of the main differences being the sensing mechanism. The sensor presented here uses changes in intensity of the optical signal to monitor changes in battery chemistry, while that in the patent is based on frequency shifting, which is generally more complex and costly.

The sensor presented here aims to improve on the methods described above by providing an accurate, real-time estimate of the SOC at a low cost. Both the sensor and the equipment necessary to read the

signal are simple and can be produced cheaply. By sensing the internal state of the battery directly the sensor provides feedback in real time and does not require significant computational capacity to convert the output to an SOC estimate.

## 2.2 Optical Properties of Li-ion electrodes

The SOC of the battery depends on internal changes in the battery chemistry. One of the aspects of these changes that has been studied is the change in optical properties during lithiation of, or the intercalation of Li ions into, the graphite electrode. Optical spectroscopy has been used to characterize graphite electrodes since the 1970s. Some of the earlier works studied synthesized lithium intercalated graphite [24]–[26]. Spectroscopy was performed on pure graphite and on graphite intercalation compounds in wavelengths ranging from about 200 to 3000nm. These studies show that the reflectivity of graphite changes with different levels of lithiation. This indicates that it may be possible to use optical spectroscopy to determine the state of lithiation, which is directly related to the SOC.

More recent work has been done by Xie and Lu with specially designed half cells featuring a window that provides a view of the graphite electrode [27]. In this study spectra were obtained of the graphite electrode that showed general agreement with earlier results presented in [26] for the more limited range of 200-800nm. This showed that the new method could be used to monitor characteristics of the graphite intercalation compound in-situ during active charge and discharge.

Harris *et al* used a windowed cell to study the progression of the lithiation reaction through the electrode [28]. This study showed that the colour of the electrode changes with state of lithiation, progressing from the initial grey through blue, red and gold. There were relatively sharp boundaries between the colours corresponding to the distinct lithiation stages. The colour change begins at the current collector and progresses linearly with time to the surface of the electrode. Similar observations and conclusions were made by Maire *et al* who used a different design of a windowed cell to study the lithium ion mobility in graphite electrodes [29]. This progression of the colour change is important in considerations for placement of the sensor in the battery and for interpreting the optical output.

In a different study Maire *et al* used a windowed cell and took digital photographs of the carbon electrode of a half cell during cycling [30]. They plotted the visual colour components of red, green and blue against changes in SOC and showed a consistent change in the electrode colour with charging and discharging of the battery. The red component appeared to have the greatest change and showed a consistent, almost linear, change from 30-100% SOC. This study shows that it may be possible to estimate SOC from optical measurements of the electrodes.

In order to verify that this method is applicable to commercial full cell batteries a study was done by our group using visible near-infrared (Vis-NIR) spectroscopy, in the range of 500-900nm, on electrodes extracted from commercial $LiFePO_4$ cells. The study investigated the reflectance of the graphite and $LiFePO_4$ electrodes and found a correlation in reflectance with SOC [31]. For the cathode the reflectance did not show any consistent changes with SOC. For the anode there were significant reflectance changes with an overall increase in reflectance with increase in SOC, in agreement with both [27] and [30]. This indicates that an optical sensor placed in contact with the anode would provide a signal that could be translated to SOC.

## 2.3 Optical Sensors

The reflectance spectroscopy study and other studies referenced above show that it may be possible to estimate SOC in Li-ion batteries by monitoring optical changes in the electrodes, more specifically the graphite anode. All of the above studies performed the measurements ex-situ or used half cell batteries, which are composed of one of the electrodes paired with a Li metal electrode. These studies are useful for determining the characteristics of the electrodes and improving battery chemistries, however they do not provide a complete picture of the full cell battery as a whole. The purpose of this thesis is to develop a sensor that performs in-situ measurements of a full cell battery that can be developed for use in commercial cells. The type of sensor chosen for this purpose is a fiber optic evanescent wave sensor.

Evanescent wave sensors experience changes in the intensity of transmitted light when the refractive index or absorption coefficient of the external medium in contact with the sensor changes. The mechanism is discussed in detail in Chapter 4. These types of sensors are well-developed, they are prolific in the literature, and have been used for many different applications. Chandani presented refractive index and temperature sensors with a high sensitivity and adjustable operating point that

were simple to manufacture and implement [32]. Gaston *et al* presented temperature, humidity and pH sensors based on side polished fiber optics that had good sensitivity and were very stable over time [33]. Fiber optic evanescent wave sensors have also been used for cure monitoring [34] and for monitoring the deposition rates of thin films [35]. They have been shown to be simple and accurate compared to other technologies for these applications.

The above examples show that fiber optic sensors are versatile and applicable to monitoring optical properties of diverse materials. One application that has not been addressed for this type of sensor is solid materials that are placed in contact with the sensor, as is the case with the battery sensor presented here. The most similar application to the battery sensor is attenuated total reflection (ATR) spectroscopy. In this type of spectroscopy a sample is placed in contact with a planar crystal waveguide. Light is coupled into the waveguide such that it experiences total internal reflection and an evanescent wave is formed that interacts with the sample. The spectrum of the output light changes based on the properties of the sample.

ATR spectroscopy is an established technique for examining optical properties of materials. One of its advantages over other methods is the ease of sample preparation. The only requirement is that the sample is brought to within the penetration depth of the reflecting surface of the waveguide. It is preferable to have good contact with the surface, however it is not necessary to attenuate the optical signal [36]. This is important for the sensor developed here, as the battery is a delicate chemical environment that cannot be altered without impacting performance and therefore the sensor must be able to sense the environment as-is, without the need the modify it.

In the application presented here the fiber optic takes the place of the planar waveguide, the battery electrode takes the place of the solid sample, and the principles of ATR apply. For the electrode samples the pliability and surface roughness determines the contact area with the sensor and the degree of attenuation. Pressure can be used to improve the contact. Another option, studied in [37], is to apply a liquid at the interface to improve the optical contact. In the battery case the electrolyte acts as an additional liquid layer. Its properties would need to be taken into account when processing the overall signal.

A fiber optic sensor based on the principles of ATR spectroscopy and evanescent wave sensing is a good candidate for monitoring the optical properties of battery electrodes. Based on the literature, this kind of sensor can be fabricated to be simple and inexpensive and has the potential to achieve high sensitivity and accuracy. The specific design considerations for applying the sensor to battery electrode monitoring are discussed in the following chapter.

# Chapter 3
# Background and Design Considerations

This chapter describes the design considerations for the sensor and examines how each one is met. First, the challenges of the internal battery environment and the limitations they place on the sensor are discussed. Several options are considered for coupling the light to the electrode and for the method of signal modulation. Finally, the geometrical parameters of the sensor and its placement in the battery are examined.

## 3.1 Battery Environment

The environment of the Li-ion battery poses several challenges to the insertion of a sensor for direct sensing of the chemistry. First, is the chemical compatibility of the sensor material. This is important both for the integrity of the sensor and for the performance of the battery. The batteries used here have an electrolyte composed of a $LiPF_6$ solution in dimethyl carbonate (DMC) and ethylene carbonate (EC), which is typical of Li-ion batteries. DMC is a strong solvent and reacts with many materials. If the sensor material is reactive to DMC it could corrode the sensor and also change the internal chemistry of the battery. In commercial batteries the proportions of the materials and chemicals used is closely controlled to maximize performance and any disruption could have a detrimental effect. Therefore, any parts of the sensor that are in contact with the inside of the battery must be inert to the chemicals present.

A second consideration for the sensor design is the physical dimension of the sensor. Li-ion batteries are composed of multiple sheets of electrodes and separators that are pressed together. The pressure is controlled such that there is optimal contact between the layers while not damaging the battery. Inserting anything between the layers will affect the amount of contact and the movement of particles, particularly ions, between the layers. For this reason the footprint and the thickness of the sensor must be minimized to reduce the impact of the sensor on the battery.

## 3.2 Inserting a Sensor into the Battery

The concept of the sensor is to monitor optical changes in the electrodes of the battery. This requires light to be delivered to the sample and then guided back to a reading instrument. A light waveguide

can be made from many different materials and can have different shapes. Optical fibers are a commonly used waveguide and are readily commercially available. Fiber optics are made from plastic or silica (glass). Experiments in the lab showed that the electrolyte reacts with some kinds of plastic, therefore silica fibers were chosen to avoid potential reactions. Silica is inert to the electrolyte and does not interfere with the battery chemistry.

The other consideration is the size of the sensor. This is a tradeoff between impacting the battery performance and ease of handling of the fiber during fabrication and battery assembly. One reason to choose a larger fiber is increased strength. The process of inserting the fiber into the battery can be difficult and the stronger the fiber, the greater the chance that it will not break. The electrodes each have a thickness of 100µm and the separator has thickness 20µm. A fiber diameter of approximately 100µm was chosen for the sensor. This has a small footprint compared to the total area of the battery and the thickness of the electrodes and separator allow for sufficient compression to maintain electrode contact throughout the battery. The effect of the fiber on the battery was tested and is discussed in Section 5.5. There are also optical considerations relating to the size of the fiber and these are discussed in Section 3.5.

## 3.3 Signal Transmission

There are several possibilities for the design of a fiber optic sensor. The two main design choices are intrinsic or extrinsic sensing, and the method of modulation. Figure 1 illustrates the differences between intrinsic and extrinsic sensors. In intrinsic sensors the light remains inside the fiber and the measurand affects the properties of the fiber to modulate the guided light. In extrinsic sensors the light leaves the input fiber, interacts with the sample, and is carried back to the detector through the output fiber, which may be the same as the input fiber. In extrinsic sensors the fiber acts mainly as a signal carrier and some method is required to couple the light to the sample and back to the output fiber.

Given the physical space constraints and the chemical compatibility constraints inside the battery the extrinsic method would be very difficult to implement. The fiber lies parallel to the measurand of interest, which is the electrode, and guiding the light in such a way as to have it reflect off the electrode poses some challenges given the limited space. One possibility, illustrated in Figure 2a), is to cleave the fiber end at an angle, which will reflect the light so that it exits the side of the fiber. The

light would reflect off the electrode and the signal would be carried back along the same fiber. This and other methods of coupling involve very fine fabrication and challenges in terms of alignment during assembly. A single fiber acting as input and output avoids alignment issues, but requires bifurcation of the fiber, which results in only half of the output signal being available to the detector.

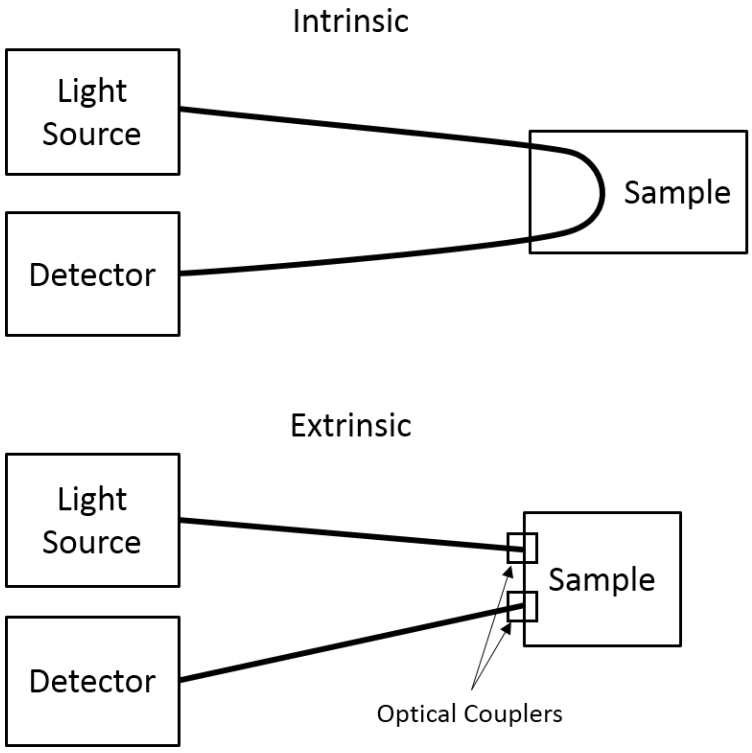


**Figure 1: Comparison of intrinsic and extrinsic fiber optic sensors. In intrinsic sensors the light remains inside the fiber while interacting with the sample. In extrinsic sensors the light interacts with the sample outside of the fiber.**

An intrinsic sensor avoids the need for coupling the light out of and into the fiber and in this way is simpler for the current application. There are two ways to realize the intrinsic sensor. In both cases there is a sensing region where the light being guided in the fiber is modulated by contact with the external medium. In one realization, illustrated in Figure 2b), the light would enter and exit the fiber at the same end, and a reflective coating at the other end, located past the sensing region, would return the modulated light back along the fiber. This, as with the single-fiber extrinsic sensor, would require a bifurcation or some other method of separating the input from the output and would result in

a lower proportion of the output signal being available at the detector. The advantage of this configuration is that only a single entry point is required into the battery, which can simplify assembly and reduce sealing issues, however this is only a minor advantage.

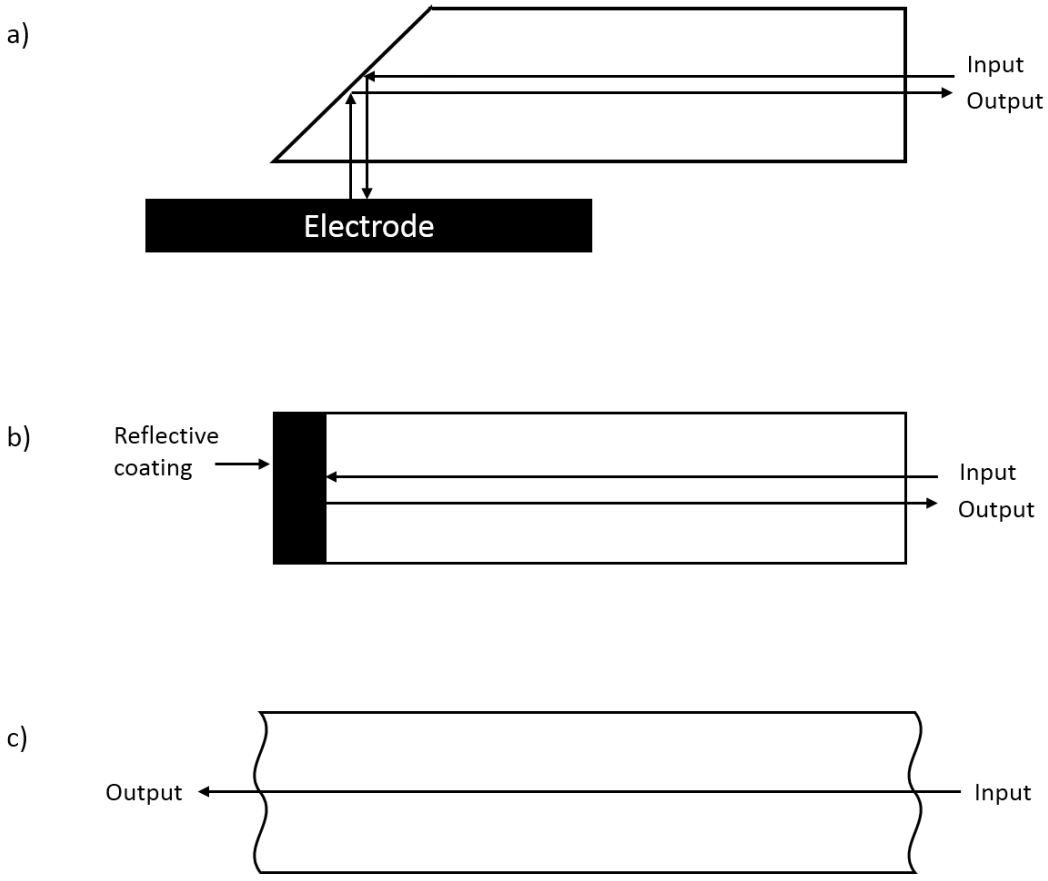


**Figure 2: Possible realizations of the fiber optic battery sensor: a) Extrinsic sensor based on a cleaved fiber, b) Intrinsic sensor where light is reflected from the end of the fiber, c) Intrinsic sensor where light is transmitted through the fiber.**

The alternative configuration, shown in Figure 2c), is to have the light enter the fiber at one end and exit at the other – the light is transmitted through the fiber and modulated along the way at the sensing region. This configuration simplifies the equipment needed to couple the light to the source and detector, as simple fiber optic connectors can be used on each end to couple to each device. There is also no need for a reflective coating material, which would have to be compatible with the battery chemistry. The disadvantage is that sealing is slightly more difficult, as the fiber enters the battery at

two points, which need to be relatively distant from one another to avoid bending the fiber excessively. This is a minor difficulty given the alternative options, and this configuration was chosen for the sensor as the simplest and most practical.

## 3.4 Signal Modulation

The sensor configuration is influenced largely by the nature of the environment in which it must function, in this case the battery. The choice of signal modulation method involves a different set of considerations. The main alternatives are phase, wavelength and intensity modulation. Phase-based sensors use two fibers and detect changes in phase between the two signals. This is also known as interferometric sensing and there are several configurations that can be used, with the four main ones being Fabry-Perot, Michelson, Mach-Zender and Sagnac. A beam splitter and combiner is required for all of these configurations. Wavelength-based sensors employ a periodic grating, such as a Bragg grating, that selectively reflects a single wavelength of light. The reflected peak shifts with changes in the measurand. A spectrum analyzer is required for this type of sensing to detect the wavelength shifts. Intensity-based sensors measure the amount of power that is lost as the light travels through the sensor, which can be due to transmission, absorption, reflection and scattering within the sensor. Intensity measurements can be done with a basic photodetector.

Each of these modulation methods can be realized in an intrinsic transmission sensor. The tradeoff is between, on the one hand higher signal sensitivity and immunity to noise factors, and on the other hand simplicity and lower cost. Phase-based and wavelength-based sensing can achieve higher sensitivity than intensity-based sensing, but require more complex optics and detectors. An optical structure, such as a grating or cavity must be fabricated in the fiber for phase- and wavelength-based sensing, while intensity-based sensors can be as simple as an unclad fiber, which is less costly to fabricate. Intensity-based sensors can be excited by a narrow band source or a wide band source, depending on the application, and the detector does not need to discern the intensities of individual wavelengths, but rather the overall intensity of the light incident upon it. Phase- and wavelength-based sensing requires a spectrum of wavelengths to be generated by the source and a detector that is capable of measuring this spectrum, which is inherently more complicated and costly than intensity measurement [38]. The drawback to intensity-based sensors is that they are more affected by external factors not related to the property that is to be measured, such as temperature changes, mechanical

changes in connectors and alignment, and bending losses [39]. These problems can be resolved by using established compensation techniques [40]. An intensity modulated sensor based on a fiber with reduced cladding was chosen for the sensor as it is simple to fabricate and uses a low cost light source and detector, which meets the objective of low cost sensing.

## 3.5 Sensor Geometry

The fiber optic evanescent wave sensor requires that the cladding of the fiber is partially removed so that the external medium can be placed within the penetration depth of the light carried by the fiber core. There are several ways to accomplish this. Side-polishing is one method for fabricating evanescent wave sensors from fiber optics [41]. With this method the fiber is typically embedded in a block, to hold the fiber and prevent breaking, and polished until the desired thickness of cladding remains. The resulting fiber is illustrated in Figure 3a). The challenge with this type of sensor is that the orientation of the fiber matters and it is very difficult to ensure proper orientation during the assembly of the battery cell. For the battery sensor the fiber ideally has uniform cladding thickness in all parts of the sensing region such that it can be placed in any orientation and produce the same result. This is accomplished by wet etching the fiber, which reduces the cladding uniformly all around the fiber, as illustrated in Figure 3b).

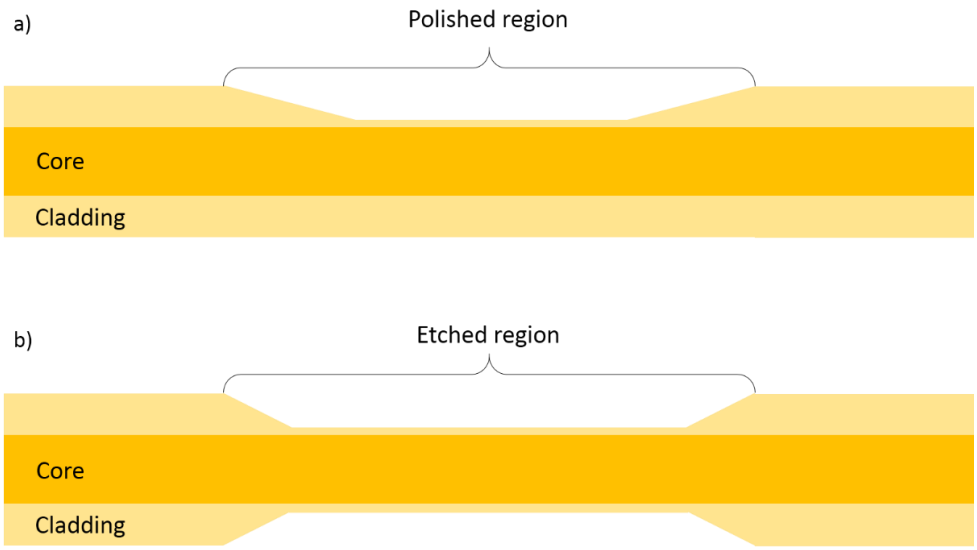


**Figure 3: Illustration of side-polished fiber (a) and etched fiber (b) showing the sensing region as either polished or etched.**

Another consideration is between a single mode fiber and a multimode fiber. Single mode fibers have a very small core, typically under 10μm, while multimode fibers come in a variety of core sizes, typically greater than 50 μm. As was discussed in Section 3.2, a larger fiber eases the process of battery assembly. Using a single mode fiber for the evanescent wave sensor would make the sensor extremely thin and therefore difficult to handle. The main advantage of single mode fiber is that it has lower dispersion and attenuation, which makes it very useful for telecommunication. For this sensor the fiber lengths are very short and single mode fibers do not provide any advantage. On the other hand it is much easier to couple light into a larger, multimode fiber, which allows for less expensive coupling optics. A larger fiber also carries more light, which increases the level of the output signal, thus increasing the signal-to-noise ratio. This further simplifies the detection equipment as noise reduction becomes less important.

In order for the evanescent wave to interact with the external medium the cladding thickness must be on the order of a wavelength. This is examined in more detail in Chapter 4. The sensor developed here uses wavelengths in the near infrared region, which means that the cladding should be around 1μm thick. Thinner cladding results in greater sensitivity as more of the evanescent wave interacts with the sample, however if there is too much attenuation then the signal-to-noise ratio will be lower, which decreases the resolution of the output signal. This was considered in the sensor design and the optimal value was arrived at based on experimental results where the greatest sensitivity was observed.

A similar tradeoff applies to the length of the sensing region. Too little length will not provide sufficient interaction with the sample, and too much will result in very low output that is difficult to detect. In the case of the battery sensor the upper limit of the length is determined by the size of the battery as the sensing length should be entirely covered by the electrode to avoid external influences on the signal. The batteries used here are very small and this was the main constraint on the length of the sensor. The maximum length was not such that there would be excessive attenuation of the signal and the sensor was made to cover the entire length of the electrode.

## 3.6 Sensor Placement and Wavelength Selection

The choice of sensor placement and wavelength is based on the results of the reflectance spectroscopy study performed by our group on electrodes extracted from commercial batteries [31]

and first discussed in Chapter 2. In this study commercial cells were charged to different SOC, then electrode samples were obtained from each cell. The reflectance of each sample was measured with a spectrometer with a range of 500-900nm. The reflectance vs. SOC for four different wavelengths is shown in Figure 4 for the graphite anode and in Figure 5 for the $LiFePO_4$ cathode. This data is from one set of samples, and is the average of three measurements that were taken at slightly different locations on each sample. The cathode does not experience consistent changes in reflectance relative to SOC at any of the observed wavelengths. The anode shows a consistent increase for higher wavelengths, with the greatest change at 850nm. Based on these results the sensor is placed next to the anode, as it is the electrode with the greatest change in reflectance, and a source at 850nm is used for the sensor signal. The choice of wavelength was verified with in-situ experiments which are discussed in Section 5.6.

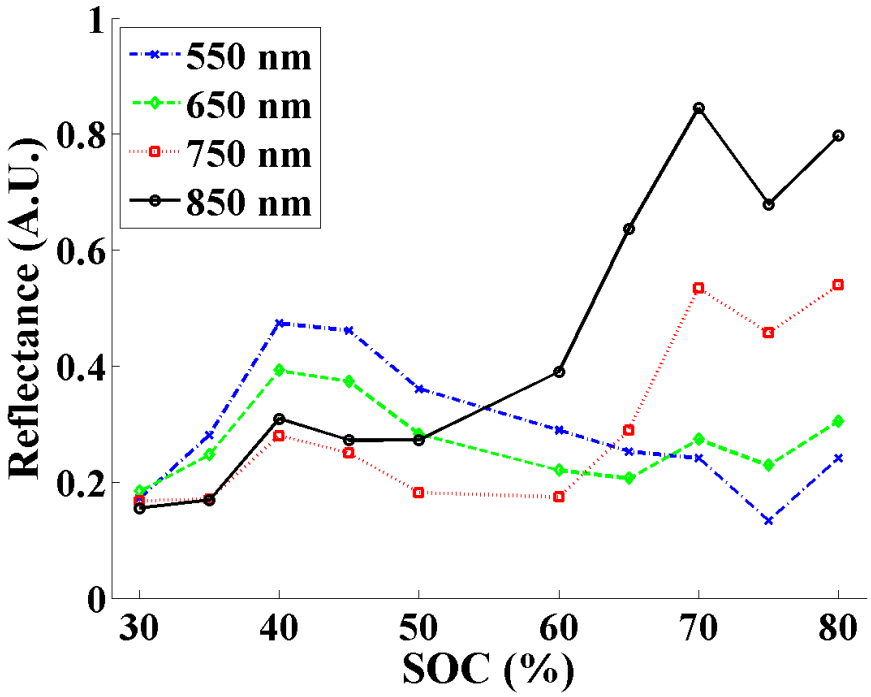


**Figure 4: Reflectance vs. SOC at different wavelengths for graphite anodes extracted from commercial $LiFePO_4$ batteries that were charged to different SOC values.**

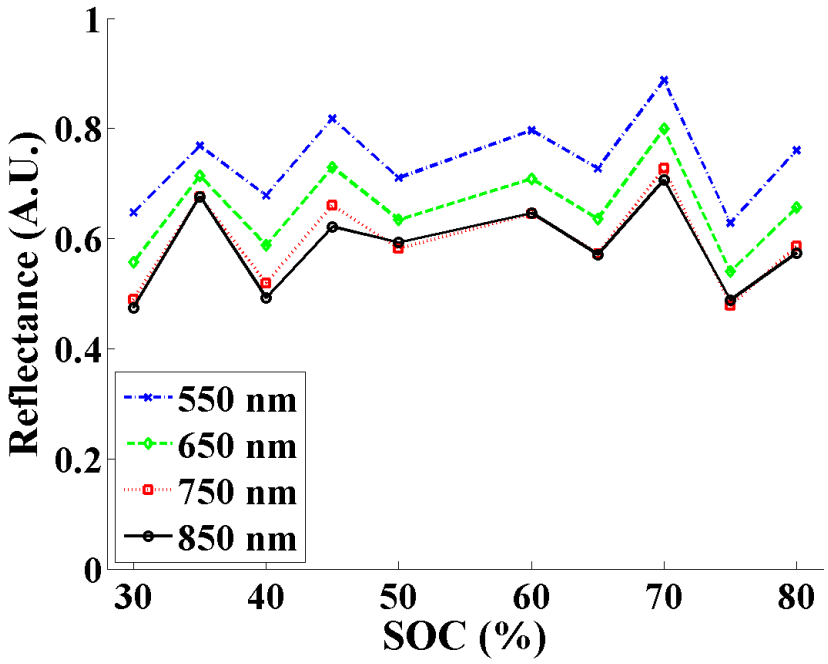


**Figure 5: Reflectance vs. SOC at different wavelengths for cathodes extracted from commercial $LiFePO_4$ batteries that were charged to different SOC values.**

## 3.7 Summary of Sensor Design

Based on the above considerations, the remainder of this thesis discusses the development of a fiber-optic sensor that will be embedded in a battery. The sensor is composed of a multimode optical fiber with a portion of the fiber etched such that the thickness of the cladding is less than 1µm. The fiber is placed inside a Li-ion battery in contact with the anode. The sensor is excited by a light source at 850nm and the intensity of the output signal is monitored. The light interacts with the electrode in the sensing region and changes in the optical properties of the electrode modulate the intensity of the signal. The theory behind this modulation is examined in the next chapter, and Chapter 5 details the fabrication of the sensor and its insertion into a battery.

# Chapter 4
# Fiber Optic Sensor Theory

Attenuated Total Reflectance (ATR) spectroscopy is an established technique for studying the properties of materials. Fiber optics can be used for spectroscopy by applying the same principles. ATR relies on evanescent waves that propagate to some depth into the sample and are partially reflected and transmitted or absorbed. In this chapter the principles of evanescent waves are discussed and applied to understanding the effects of the geometry of the fiber optic sensor. A model based on the transfer matrix method is presented for analyzing the effect of the external medium on the evanescent wave sensor. A method for relating the optical properties of the electrode to the SOC of the battery is discussed.

## 4.1 Total Internal Reflection

When light is incident on the interface between two media, some of the energy is reflected and some is transmitted. This is illustrated in Figure 6. The transmitted ray is refracted according to Snell's law:

$$n_1 sin\theta_i = n_2 sin\theta_t$$

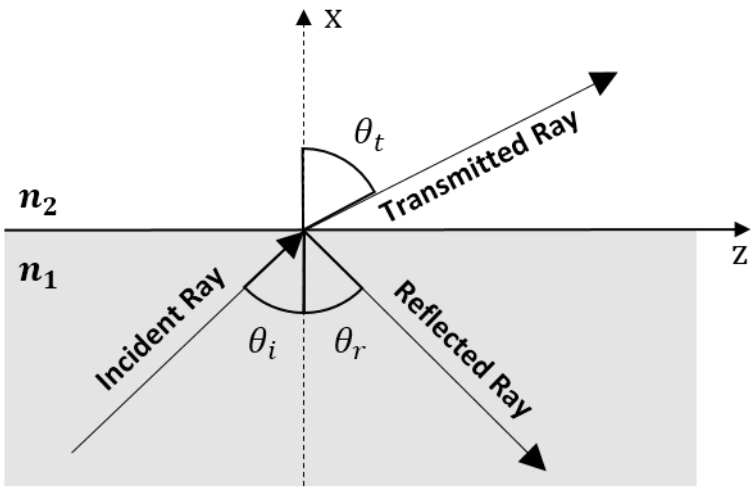


**Figure 6: Illustration of reflection and transmission of incident light at an interface between two media.**

By applying Maxwell's equations the following formulas can be found for the amplitude of the reflected and transmitted waves for perpendicular polarization, denoted by subscript *s*, and parallel polarization, denoted by subscript *p*:

$$r_s = \frac{n_1 cos\theta_i - n_2 cos\theta_t}{n_1 cos\theta_i + n_2 cos\theta_t} \tag{1}$$

$$t_s = \frac{2n_1 cos\theta_i}{n_1 cos\theta_i + n_2 cos\theta_t} \tag{2}$$

$$r_p = \frac{n_2 cos\theta_i - n_1 cos\theta_t}{n_2 cos\theta_i + n_1 cos\theta_t} \tag{3}$$

$$t_p = \frac{2n_1 cos\theta_i}{n_2 cos\theta_i + n_1 cos\theta_t} \tag{4}$$

When light is incident from a denser medium onto a rarer medium ($n_1 > n_2$), then $\theta_t > \theta_i$. In this case the reflected amplitude is always increasing until it reaches 1 at $\theta_t = 90^0$. This is known as total internal reflection, since all the light is reflected. The value of $\theta_i$ where this happens is known as the critical angle $\theta_c$, and can be found from Snell's law. To satisfy the boundary conditions there must be a transmitted field, however this field carries no energy across the boundary. The transmitted electric field is described by the following equation [42]:

$$\boldsymbol{E}_t(\mathrm{r},\mathrm{t}) = \mathrm{Re}\{\boldsymbol{E}_{0t} e^{i(\boldsymbol{k}_t \cdot \boldsymbol{r} - \omega t)}\} \tag{5}$$

where:

$$\boldsymbol{k}_t \cdot \boldsymbol{r} = k_{tx}x + k_{tz}z = k_t sin\theta_t + k_t cos\theta_t \tag{6}$$

By applying Snell's law we get:

$$k_t cos\theta_t = \pm k_t \left(1 - \frac{sin^2\theta_i}{{n_{21}}^2}\right)^{1/2} \tag{7}$$

where

$$n_{21} = \frac{n_2}{n_1} \tag{8}$$

For the case where $sin\theta_i > n_{21}$:

$$k_{tx} = \pm ik_t \left( \frac{sin^2\theta_i}{{n_{21}}^2} - 1 \right)^{1/2} \equiv i\beta \tag{9}$$

$$k_{tz} = \frac{k_t}{n_{21}} sin\theta_i \tag{10}$$

This leads to the electric field:

$$\boldsymbol{E}_t = \mathrm{Re}\left\{ \boldsymbol{E}_{0t} e^{\mp \beta y} e^{i(\boldsymbol{k_t} x sin\theta_i / n_{21} - \omega t)} \right\} \tag{11}$$

The value of $\beta$ can be positive or negative, however, the positive would imply an exponentially increasing wave, which is physically impossible. Therefore, the transmitted wave has an amplitude that decays exponentially away from the boundary. This is called an evanescent wave. An important characteristic of the evanescent wave is the distance that it penetrates into the second medium. The penetration depth is defined as the distance it takes for the amplitude to fall to $e^{-1}$ of its value at the surface and is given by:

$$d_p = \frac{\lambda}{2\pi n_1 (sin^2\theta_i - {n_{21}}^2)^{1/2}} \tag{12}$$

The penetration depth is proportional to the wavelength and is greater for longer wavelengths. It depends on the angle of incidence and increases as the angle of incidence approaches the critical angle. It is also larger when the index of the cladding is close to that of the core, as in most optical fibers.

## 4.2 Evanescent Wave Coupling

In the previous section the conditions for the evanescent wave and its characteristics were described. There are two ways that the evanescent wave can direct power away from the boundary between two media where total internal reflection occurs and perturb the total reflection. The first involves

bringing a non-absorbing medium of refractive index $n_3$, greater than or equal to the refractive index of the propagating medium $n_1$, close to the boundary and within the field of the evanescent wave. This implies that the second medium is thin relative to the wavelength. In this case a propagating wave is induced in the third medium, which carries power away from the boundary. The second way, illustrated in Figure 7, is to bring an absorbing medium within the evanescent field, which will attenuate the reflected power by absorption.

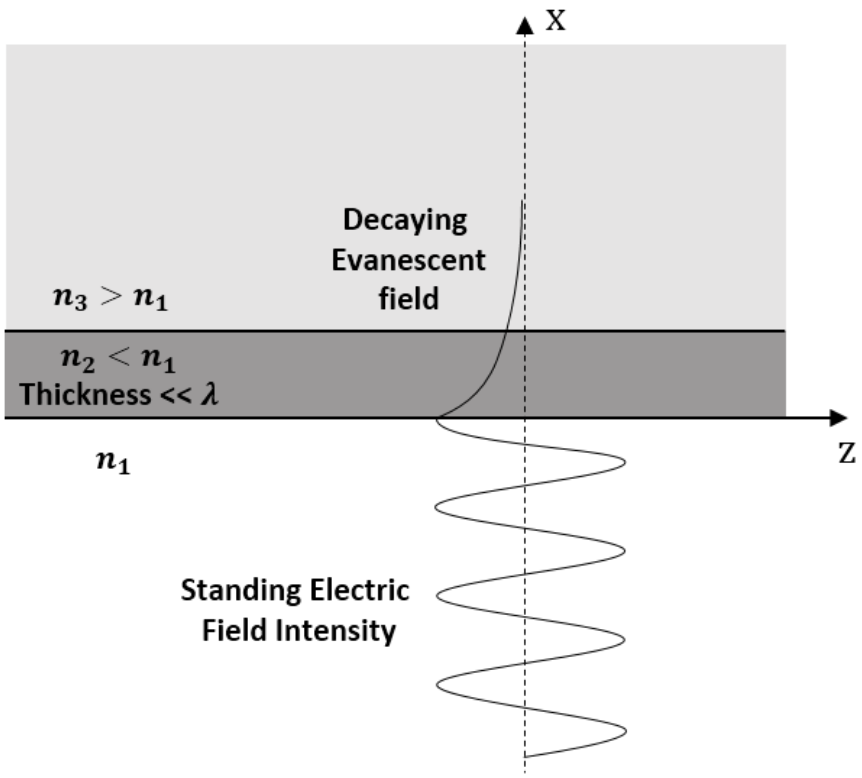


**Figure 7: Illustration of the evanescent field generated by total internal reflection at an interface between two media, one of which is a thin film, and the penetration of the evanescent field into a third medium.**

The sensor presented here consists of an optical fiber where part of the cladding, represented by the second medium of refractive index $n_2$, has been removed and replaced by an absorbing medium of refractive index $n_3$. The cladding is sufficiently thin such that the evanescent field penetrates into the absorbing medium. The power transmitted in the fiber is given by:

$$P(z) = P(0)e^{-\gamma z} \tag{13}$$

where z is the distance along the unclad region of the fiber, P(0) is the power at the start of the unclad region, and $\gamma$ is an absorption coefficient, which depends on the bulk absorption coefficient of the medium and the power that is propagating in the cladding.

## 4.3 Relationship to Sensor Parameters

The equations above give insight into the effect of various parameters on the sensor output. The two main parameters are the sensing length and the cladding thickness. From Equation 13 we can see how the length of the sensing region, or unclad region, affects the sensor output. The proportion of output power decreases exponentially as the sensing length increases. If the sensing region is very long the output power approaches zero.

The thickness of the remaining cladding affects the degree to which the evanescent wave is coupled to the third medium. The thinner the cladding the more of the evanescent field that penetrates into the third medium. The cladding thickness affects the coupling exponentially as the field decays exponentially away from the boundary. For a very thin cladding the proportion of power that is coupled is very sensitive to changes in the cladding thickness.

## 4.4 Transfer Matrix Model

The power attenuation in the fiber depends on the length and evanescent coupling, and also on the absorption coefficient $\gamma$ from Equation 13, which can be written as [43]:

$$\gamma = NT \tag{14}$$

where N is the number of reflections per unit length and T is the transmission coefficient at the interface. For two semi-infinite media, or a single interface, the Fresnel equations can be applied to find the transmission coefficient. The sensor presented here consists of three layers, namely core, cladding and external medium. A three layer stack representative of the sensor is illustrated in Figure 8, where $n_1$, $n_2$ and $n_3$ are the refractive indices of the core, cladding and external medium respectively. For multiple interfaces finding the Fresnel coefficients becomes cumbersome.

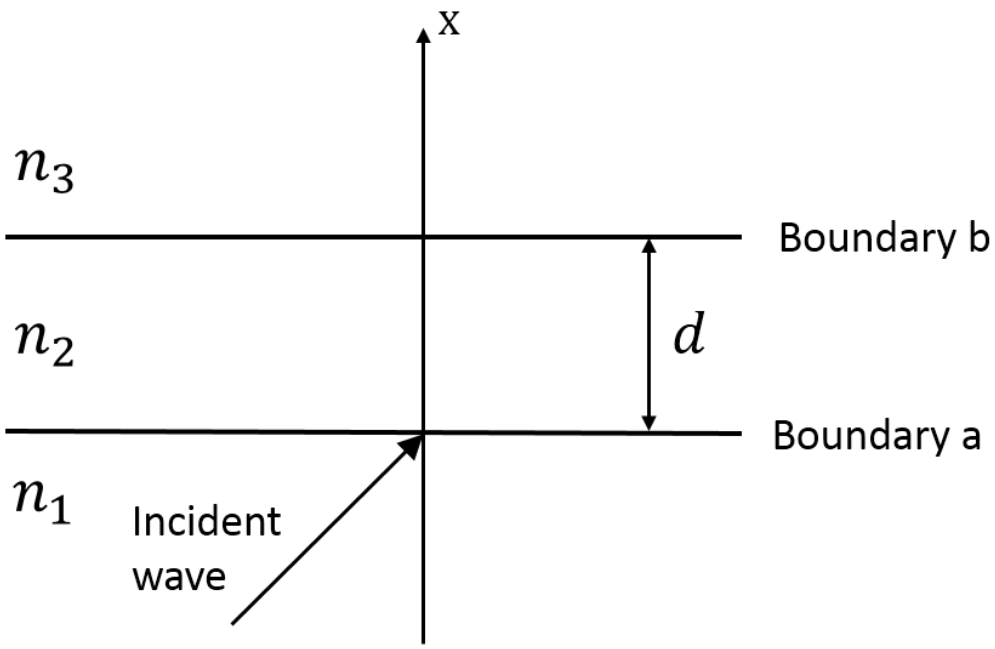


**Figure 8: Illustration of a three layer stack of optical media.**

A more elegant approach is to use Maxwell's equations and the boundary conditions at the interfaces to find the transmission coefficient. Using this approach the equations for the electric and magnetic fields for a plane wave at the two boundaries can be written in matrix form [44] (the full derivation is presented in Appendix A):

$$\begin{bmatrix} \mathbf{E}_\mathrm{a} \\ \mathbf{H}_\mathrm{a} \end{bmatrix} = \begin{bmatrix} \cos\delta & \dfrac{\mathrm{i}\sin(\delta)}{\eta_2} \\ \mathrm{i}\eta_2 \sin\delta & \cos\delta \end{bmatrix} \begin{bmatrix} \mathbf{E}_\mathrm{b} \\ \mathbf{H}_\mathrm{b} \end{bmatrix} \tag{15}$$

where $\mathbf{E}_\mathrm{a}$and $\mathbf{H}_\mathrm{a}$ are the fields at boundary a and $\mathbf{E}_b$ and $\mathbf{H}_b$ are the fields at boundary b, $\eta_2$ is the electromagnetic wave impedance in the second medium, $\delta$ is a function of the film thickness d and the angle of incidence $\theta_i$, and is given by:

$$\delta = \frac{2\pi}{\lambda_0} n_2 d \cos\theta_i \tag{16}$$

Using this the reflectance of the thin film can be written as:

$$R = \left(\frac{\eta_1 - Y}{\eta_1 + Y}\right)\left(\frac{\eta_1 - Y}{\eta_1 + Y}\right)^* \tag{17}$$

Where Y is the effective admittance of the thin film assembly and is given by:

$$Y = \frac{\boldsymbol{H}_a}{\boldsymbol{E}_a} = \frac{\eta_3 cos\delta + i\eta_2 sin\delta}{cos\delta + i\left({}^{\eta_3}/_{\eta_2}\right)sin\delta} \tag{18}$$

The transmittance into the third medium is found by $T = 1 - R$.

This model is used here to study the effects of the refractive index of the external medium on the transmittance of the thin film assembly. Figure 9 shows a plot of the transmittance where both the real, n, and imaginary, k, parts of the refractive index are varied, while the film thickness and angle of incidence are kept constant. The imaginary part of the refractive index is also known as the extinction coefficient, and when its value is zero that means that the medium is non-absorbing. For non-absorbing media the transmission is zero as long as the external medium has a refractive index lower than the cladding. At values close to the refractive index of the cladding there is a sharp increase in transmission, and a gradual decline as the index of the external medium increases further. When the medium is absorbing it can be seen that the effect of the extinction coefficient is more dominant than that of the real refractive index. As the values of n and k increase their effect on the transmittance diminishes.

## 4.5 Relationship with SOC

The model can be used to relate the optical properties of the electrode, namely refractive index and extinction coefficient, to the SOC of the battery. This relationship can be represented by the following equation, where N denotes the complex index of refraction:

$$N(SOC) = n(SOC) + ik(SOC)$$

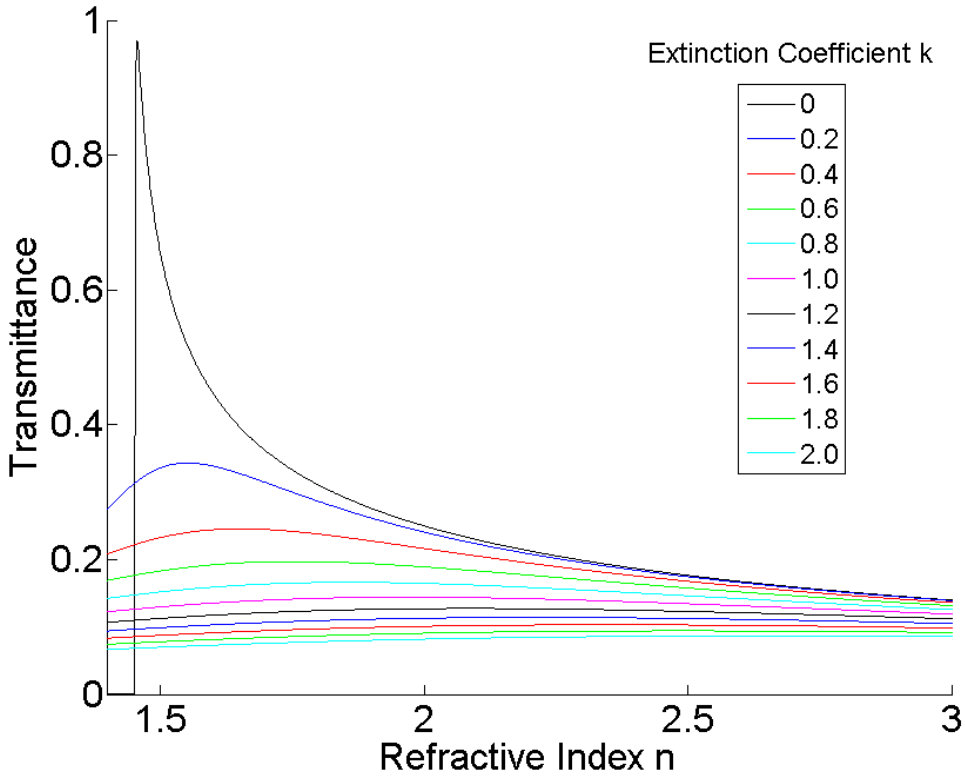


**Figure 9: Transmittance of a thin film stack for varying values of the real part of the refractive index and the extinction coefficient.**

If the refractive index values at 0% and 100% SOC were known and there was a linear change in refractive index from one to the other, then the refractive index components could be written as:

$$n = n_{0\%\,SOC}(1 - SOC) + n_{100\%\,SOC}(SOC)$$

$$k = k_{0\%\,SOC}(1 - SOC) + k_{100\%\,SOC}(SOC)$$

In reality the relationship is much more complicated. The refractive index of graphite (carbon) is known to be $N_C = 3.0761 + i1.8101$ [44]. However, precise data is not available on the refractive index of lithiated graphite. Furthermore, it may not be reasonable to assume a linear change in the refractive index. Studies in the literature [28], discussed in Section 2.2, have shown that the stages of

lithiation have distinct colours, with relatively sharp boundaries between them. The studies looked at the visible wavelengths of light, however it is reasonable to assume that the lithiation stages would exhibit distinct optical properties at other wavelengths. This implies that the equation governing the refractive index to SOC relationship may be quite complex when considering the entire SOC range.

It may be possible to derive a model of the relationship using data from the battery sensor presented here. The transmittance measured from the sensor output for different SOC values can be related to the modeled transmittance for varying refractive index values, thus giving a relationship between SOC and refractive index. Based on the distinction of colours observed in graphite at different stages of lithiation it is likely that the sensor response will exhibit distinct variations during different stages of charging and discharging of the battery. One possibility for the sensor is that may be used to study the optical properties of graphite lithiation stages. To obtain accurate representations of the refractive index would require a model that takes into account all the aspects of the fiber optic sensor system such that a quantitatively accurate value of the transmittance can be calculated and compared to measured values.

# Chapter 5
# Sensor Fabrication and Experimental Setup

## 5.1 Sensor Fabrication

The evanescent wave sensor is fabricated by etching a section of the fiber to partially remove the cladding, such that the evanescent wave can interact with the external medium. This means that the cladding thickness is on the order of a wavelength, in this case between 0 and 1µm. The fibers used to make the sensors are multimode silica fibers with core thickness 105µm and total thickness 125µm, giving 20µm of cladding (Thorlabs FG105LCA). Etching with Hydrofluoric acid (HF) is used to thin the cladding of the silica fibers.

The fibers have a polymer coating of thickness 250µm, which must be removed prior to etching. The coating is removed by scoring at two locations near the center of a 70cm length of fiber using a fiber stripper, then pressing a wipe soaked in acetone to this section for 1-2minutes to swell the coating, and removing the coating by gently wiping it with the wipe. The coating that is swelled by the acetone slides over the unaffected coating and is removed. The sensing length is determined by the length of coating that is removed, which is typically 12-14mm.

### 5.1.1 Etching with HF

Two methods are used to etch the fibers. The first one involves suspending the fiber in a droplet of HF, as shown in Figure 10a). This method could only be used to etch one fiber at a time and the etch rate was not very consistent. The droplet would crystallize due to evaporation, which resulted in the etch rate varying, depending on humidity conditions in the lab. A second method, shown in Figure 10b), was designed to improve upon this. It involves fixing the fiber in a fixture that fits onto a beaker such that the exposed section of the fiber is immersed in the HF in the beaker. This method allows for etching up to three fibers at once and also results in a more consistent etch rate as the HF is more confined and experiences less evaporation.

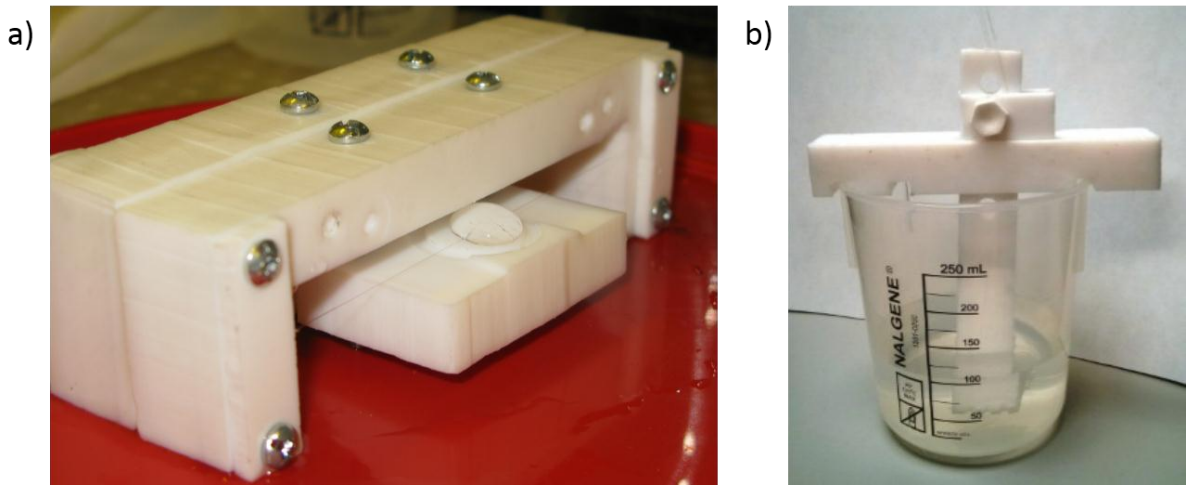


**Figure 10: Setup for fiber etching with HF: a) fiber is suspended in a droplet of HF, b) fiber is held in a fixture and immersed in HF a beaker.**

Originally, concentrated 49% HF was used to etch the fibers. Using concentrated HF has a very consistent etch rate and short etch times of less than three minutes, however, it causes damage to the fibers, making them more fragile and uneven in terms of cladding thickness. For subsequent sensors a buffered HF (BHF) solution was used with 6:1 ratio of Ammonium fluoride to HF. With BHF the etching times are around 50 minutes, and two stages have to be used – an initial etch to get close to the desired thickness, followed by characterization (described in Section 5.3), followed by an additional etch whose duration is determined based on the characterization results. Figure 11 shows SEM images of a fiber etched with concentrated HF and a fiber etched with BHF. The fibers etched with concentrated HF have a damaged surface with prominent pitting, which resulted in sensors that did not produce consistent results when used in a battery and were more prone to breaking. The BHF results in a much smoother and cleaner surface and a higher quality sensor.

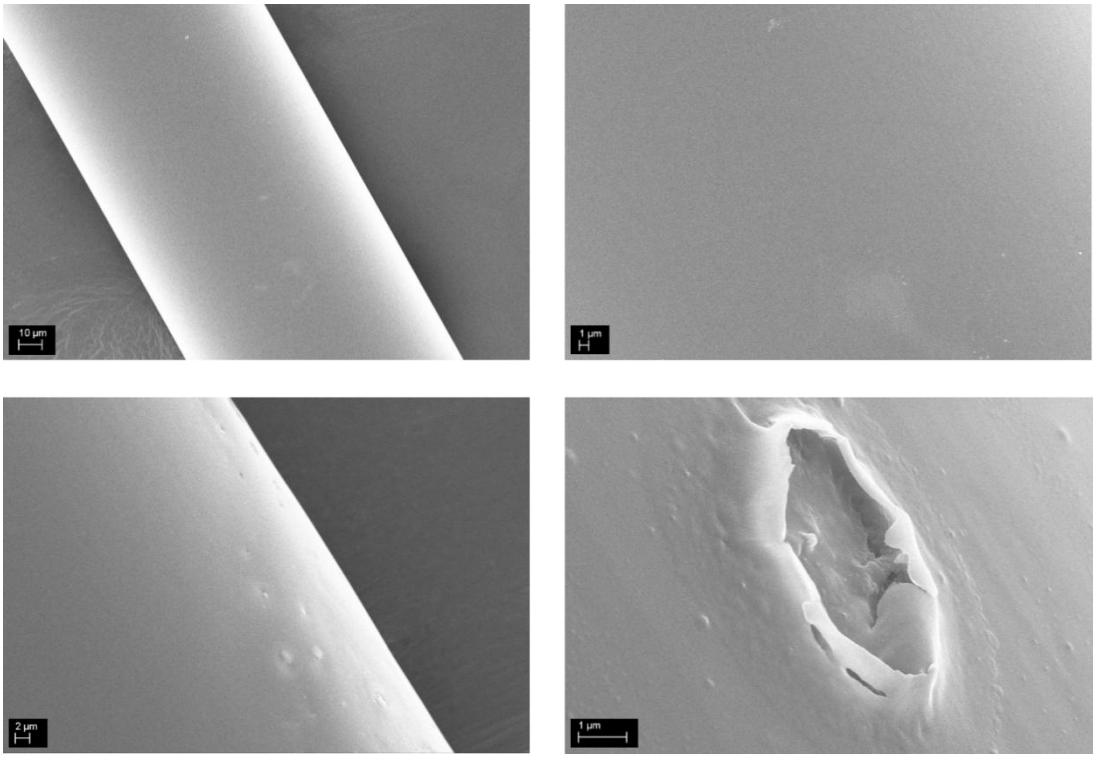


**Figure 11: SEM images showing fibers etched with buffered HF (top) and concentrated HF (bottom). Buffered HF results in a smooth surface while concentrated HF produces prominent pitting. Scale is shown in each image.**

## 5.2 Sensor Light Coupling and Detection

For coupling light into and out of the fiber standard SMA fiber connectors were used. For characterization temporary connectors (BFTU from Thorlabs) were used. For long term in-situ battery tests the connectors were applied permanently with epoxy, as the temporary connectors were more prone to signal shifts and noise due to physical shocks and vibrations.

Two systems were used to interrogate the sensor signals. The first, illustrated in Figure 12, consists of an LED (VSLY5850), with a center wavelength of 850nm, and an InGaAs photodetector (Thorlabs DET10C). The fiber connectors are coupled to the LED and photodetector with adaptors (Thorlabs SM1SMA and S120-SMA). The LED is connected to a power supply and the photodetector signal is read with an oscilloscope, which is connected to a computer for data acquisition. The second optical

signal acquisition system was developed in the lab and called the Optical Signal Interrogator (OSI). It uses a fiber transmitter (OPF370A) and photodetector (OPF480), as well as signal amplification circuitry, and is incorporated with an Arduino board for reading the signals and recording the data.

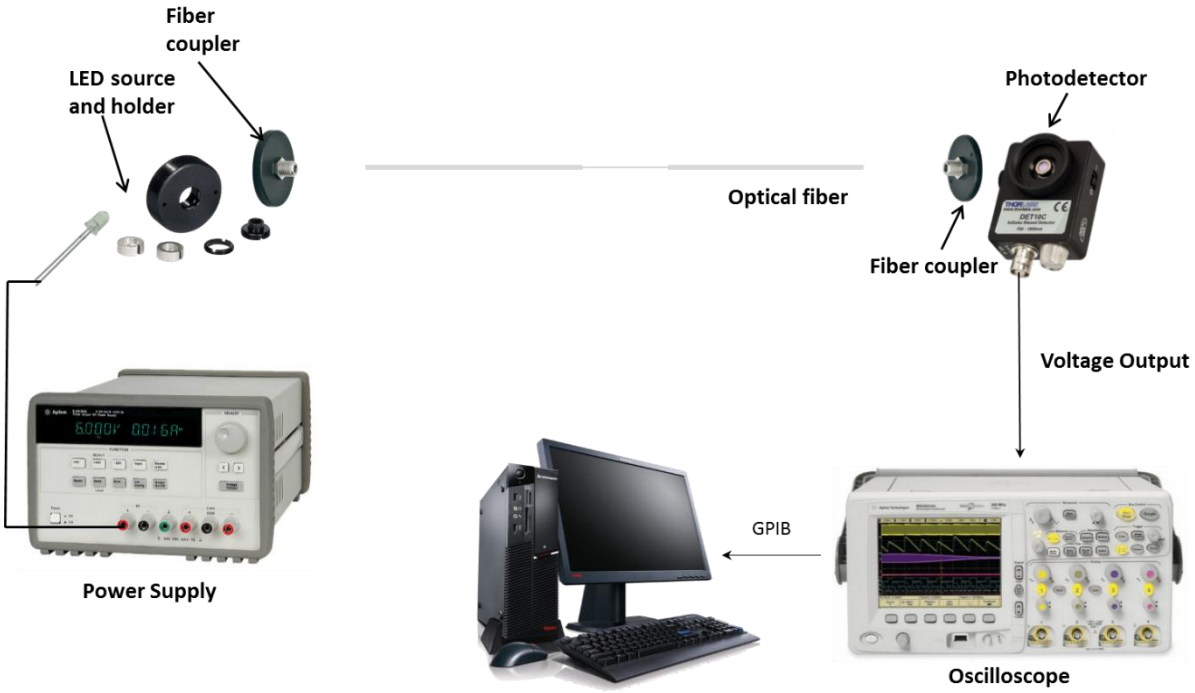


**Figure 12: Illustration of setup used to acquire the optical signal from the sensor. The sensor is excited by an LED and the signal is read by a photodetector connected to an oscilloscope.**

## 5.3 Sensor Characterization

Following fabrication the sensors are characterized to provide a measure of the cladding thickness and sensitivity of the sensor. First, optical microscopy is used to give an approximate measure of the cladding thickness. Images of the etched fiber under an optical microscope at 400x magnification are compared with a reference fiber of known thickness. The reference is an unetched fiber, which is assumed to have a thickness of 125µm based on the datasheet. A simple calculation yields the total thickness of the etched fiber. Assuming a core thickness of 105µm, the cladding thickness is calculated. This method has a very low resolution and cannot reliably be used to measure sub-micrometer dimensions, which is necessary since the required cladding thickness is less than 1µm.

The same method was attempted with SEM images of the fiber, but it was also found to not have sufficient accuracy as the thickness has slight variations along the length of the fiber.

A second method is used to more precisely characterize the sensitivity of the sensor. This involves immersion of the fiber in glycerol, a medium of high refractive index, and measurement of the change in output power. For this testing temporary connectors and the LED/photodetector system are used. Figure 13 shows this setup with a fiber whose sensing region is immersed in glycerol. The first step of the test is to measure the output of the fiber when the sensor is in air (refractive index of 1). The second step is to immerse the sensor in glycerol (refractive index of 1.465 at 850nm [45]) and measure the change in output.

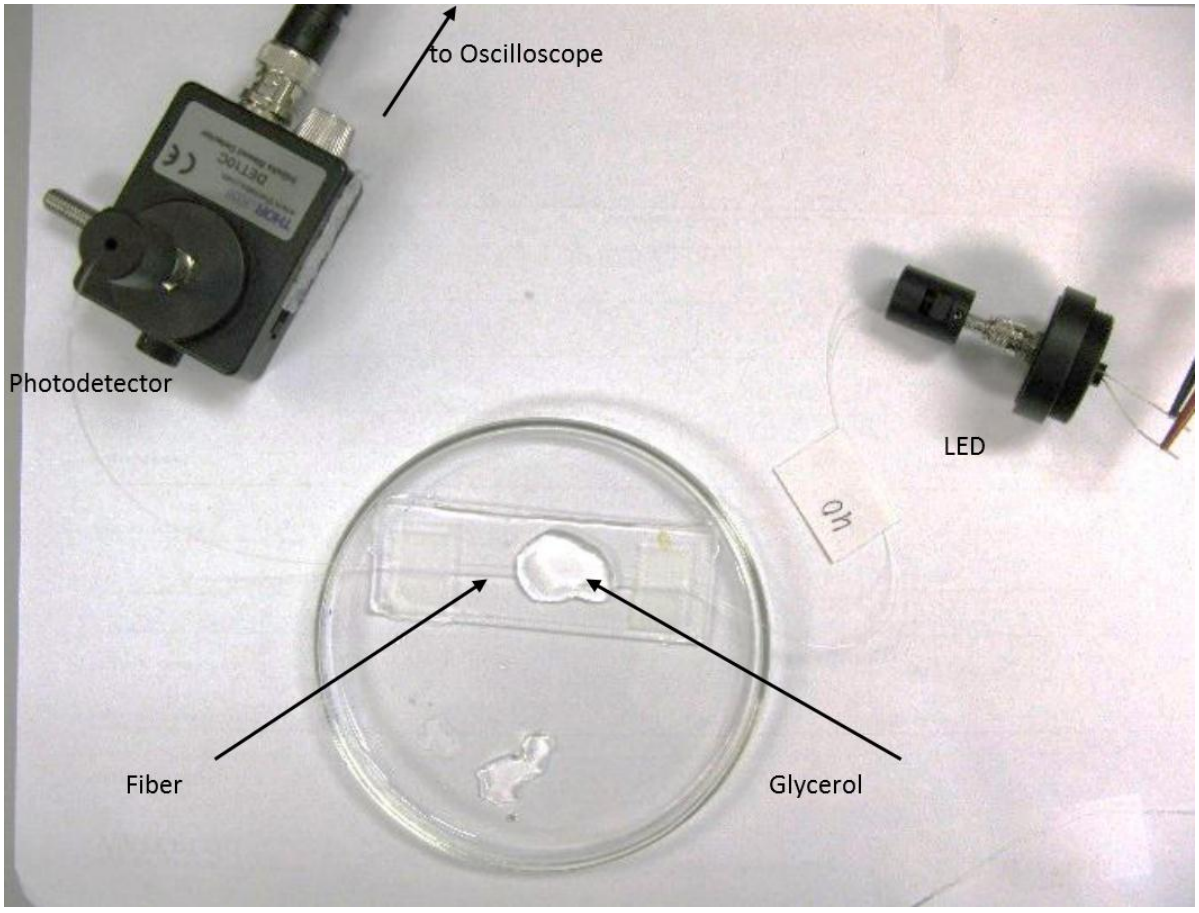


**Figure 13: Glycerol test setup showing fiber immersed in glycerol, as well as LED and photodetector used to generate and measure the optical signal.**

The amount of power lost from air to glycerol is used as a measure of the sensitivity of the sensor. Since air has a lower refractive index than the cladding of the fiber there is no power loss in air and it behaves as if the full cladding is still present. Applying a medium of higher refractive index causes losses in the fiber. The losses depend on the cladding thickness and the length of the sensing region. Following several in-situ battery experiments (described in the following sections) the optimal loss for having the maximum signal in the battery was found to be 85-90%.

The glycerol test does not give entirely accurate results as variations of up to 5% were observed between subsequent tests of the same sensor. Glycerol is prone to contamination due to absorbing moisture from the air and each sample may differ slightly in refractive index. This issue can be overcome by using a calibrated refractive index oil, which would have a more consistent and precisely known refractive index.

## 5.4 Insertion of the Fiber Optic Sensor into a Battery

In order to monitor optical changes in the battery while it cycles the sensor must be incorporated into a working battery. Several alternatives were considered for fabricating the cell, including a button cell, Swagelok cell and inserting a sensor into a pre-made commercial cell. The main issue with Li-ion batteries is that they must be sealed to avoid contamination with air, as oxygen and humidity react with lithium and degrade the battery. Button cells are relatively easy to make and can be sealed very well, however these cells have a metal shell and it would be very difficult to incorporate channels such that the fiber can be inserted into the cell. Commercial cells would have to be opened and resealed around the fiber and this was a challenge that could not be met with the available equipment. The best option was decided to be the Swagelok cell, which is sometimes used for prototype batteries.

A modified plastic Swagelok® fitting (PFA-820-6) is used to create a battery with incorporated fiber. A hole is made in the fitting to allow the fiber to pass through. Figure 14 shows a cross-section diagram of the assembled cell. The battery is contained between two steel cylinders that act as the battery terminals. They are designed such that one aligns with the fiber port and the other moves freely to allow for sufficient pressure to be applied to the battery so that there is good contact between all the components. The second cylinder, which is on the anode side of the battery is rounded to avoid pinching the fiber in the area where it is not covered by the electrode.

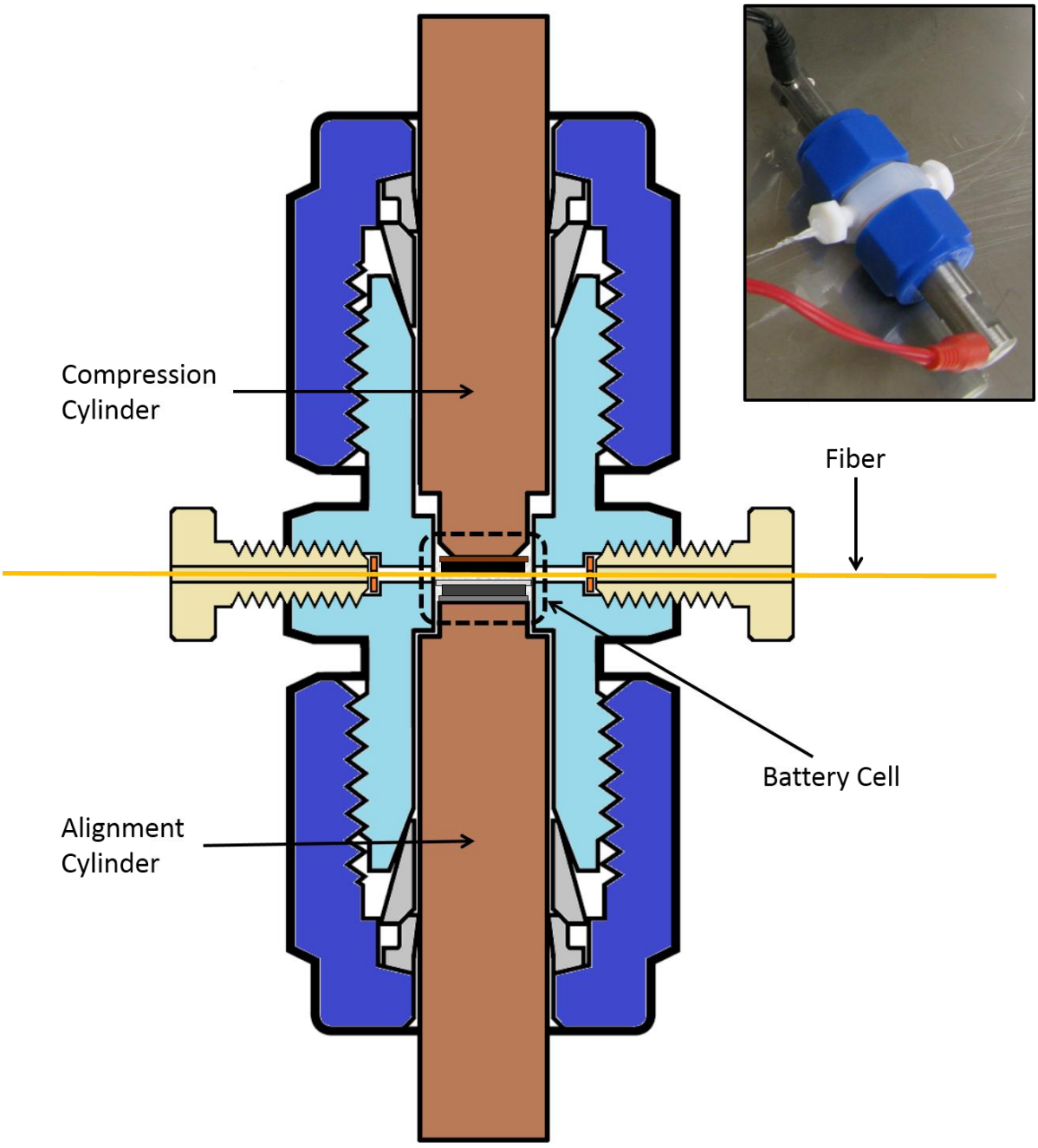


**Figure 14: Schematic of Swagelok® battery cell with incorporated fiber. The battery cell composed of the two electrodes and separator is held in the middle between the two cylinders that act as battery terminals. The fiber is guided through ports on either side that are sealed with gaskets and screws. Inset shows a photograph of an assembled cell.**

One advantage of the Swagelok cell is that it is designed to provide a good seal around the battery terminal cylinders, which is one source of leaks. The other source of leaks is the fiber port. This was sealed using gaskets and screws, seen in Figure 14. It was found that the fiber seal deteriorated when the cell was reused to build multiple batteries. Due to the cost of using new Swagelok fittings for each experiment the cells were kept in a nitrogen atmosphere during cycling in order to prevent contamination with the air and to extend the life of the battery. The cells were assembled in an argon glove box, then transferred to a nitrogen glove box in resealable plastic bags. This procedure minimized contamination and allowed for sufficient battery life for the cells.

Figure 15 shows a schematic of the composition of the battery, including the position of the sensor. The fiber sits between the anode and separator, with the cathode on the other side of the separator. The cathode is LiFePO4 (MTI bc-af-241lpf-ss) and the anode is graphite (MTI bc-cf-241-ss). The sensor is in contact with the anode, which was shown in studies to have greater optical changes. It is also in contact with the separator and electrolyte.

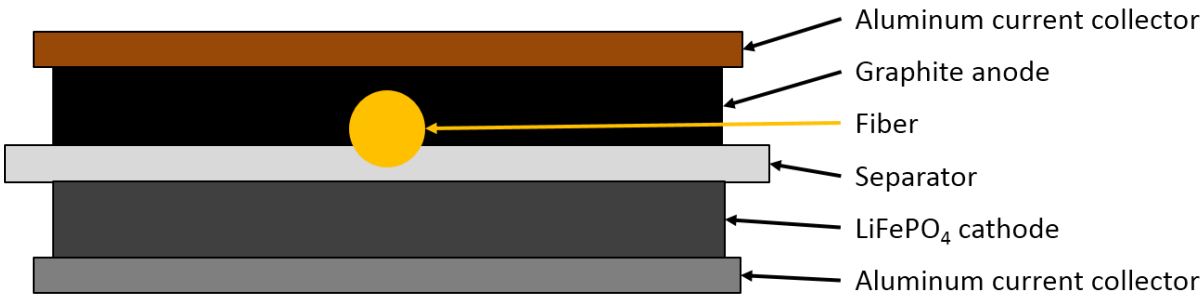


**Figure 15: Illustration of battery cell showing fiber position.**

### 5.4.1 Battery Cycling Protocol

For all experiments presented in this thesis the battery cells were cycled using the same protocol, which was a Constant Current (CC) charge and discharge. For batteries the C-rate is a measure of the rate of charging and discharging, where 1C is defined as the current that fully charges the battery in 1 hour. A low C-rate of 0.1C was used here in order to prolong the life of the cells. For the batteries used the voltage limits were from 2.5V to 3.7V, where a potential of 2.5V across the battery terminals

was defined as indicating 0% SOC and 3.7V was defined as indicating 100% SOC. The capacity of the cell is defined as the maximum amount of charge that it can currently hold. In all battery cells the capacity decreases gradually as the cell ages. For the laboratory made batteries used here the capacity decreased at a much faster rate than in would in commercial cells. The initial charge would take 10 hours, with a sharp decrease for the second charge, and a gradual decrease in capacity thereafter. In between charging and discharging the cell was rested for 20 minutes with no current applied during this time.

## 5.5 Impact of Fiber on Battery Performance

One of the requirements of the cell is that the fiber does not impact battery performance. To verify that the battery would function normally with a fiber inside, two cells were made where one had a fiber and one did not. The fiber used was a bare fiber that is the same as that used for the sensor, except that it was not etched and was therefore slightly larger than the sensor, but not significantly so. Both cells were made in Swagelok fittings with the same electrodes, separator and electrolyte. Figure 16 shows the voltage and current profile for these two cells. There are slight differences in the battery capacity. The non-fiber cells has longer cycles that indicate higher capacity, but this can be attributed to variations in the manual assembly process. The voltage profile is not affected and the overall performance of the fiber battery does not show significant differences from the fiber cell to the non-fiber cell.

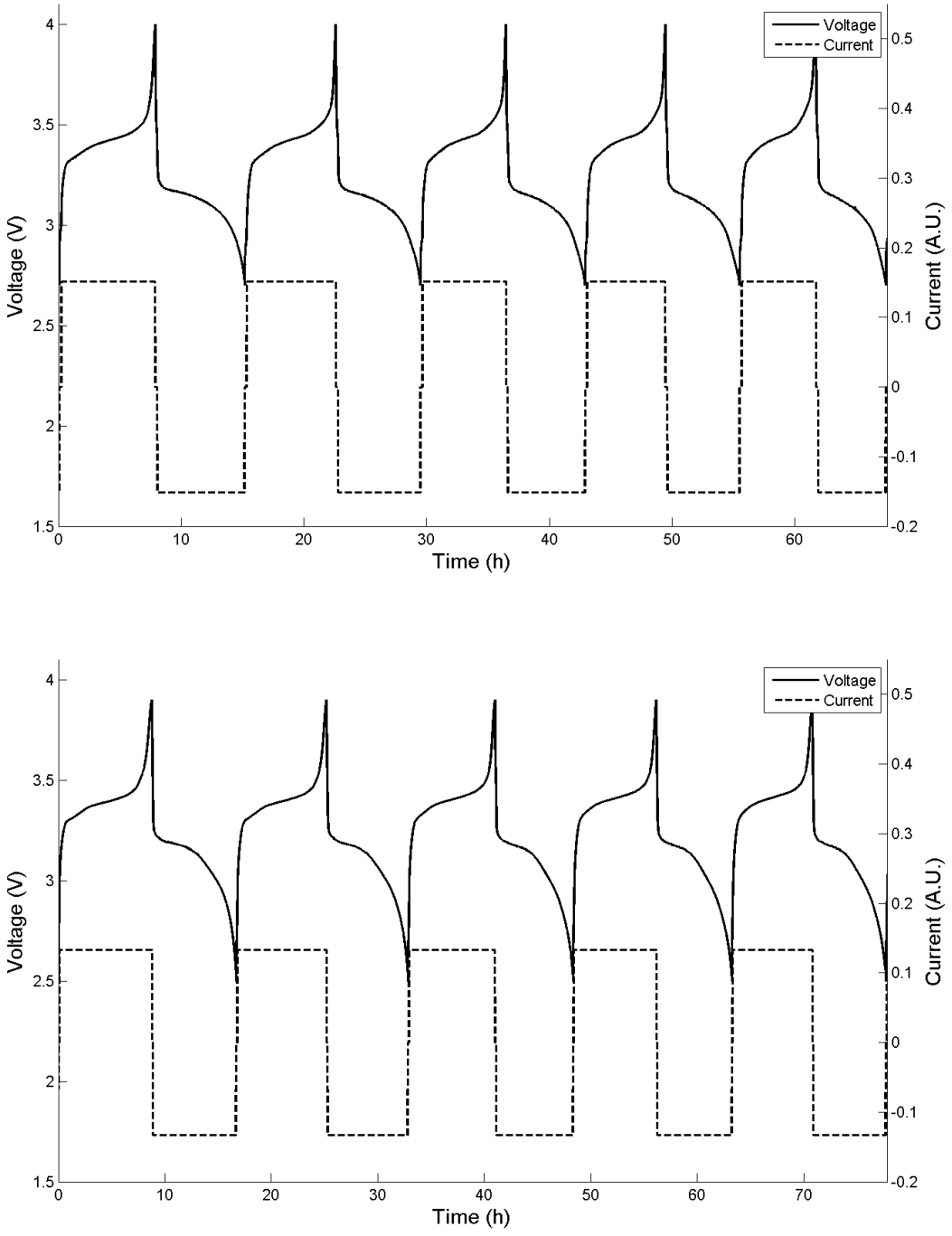


**Figure 16: Voltage and current curves over time for five charge and discharge cycles from a cell that incorporates a fiber (top) and a cell without a fiber (bottom).**

## 5.6 Spectrometer Testing and Wavelength Confirmation

Once the sensor was fabricated and successfully inserted into a working battery the first step was to confirm the wavelength selection. This was done by exciting the sensor with a white light source and using a spectrometer (Ocean Optics USB4000) to measure spectrum data of the output in the wavelength range of 500-900nm. The cell that this sensor was embedded into was cycled using the protocol described above. Figure 17 shows the transmittance over time at several wavelengths, encompassing about 11 battery cycles. The transmittance at 850nm shows the greatest change between the charged and discharged state of the battery. This confirms the results of the reflectance spectroscopy done previously by showing that the greatest optical changes occur at wavelengths close to 850nm. This wavelength is used for subsequent experiments, which are used to analyze the relationship between the transmittance and SOC of the battery, and are described in the next chapter.

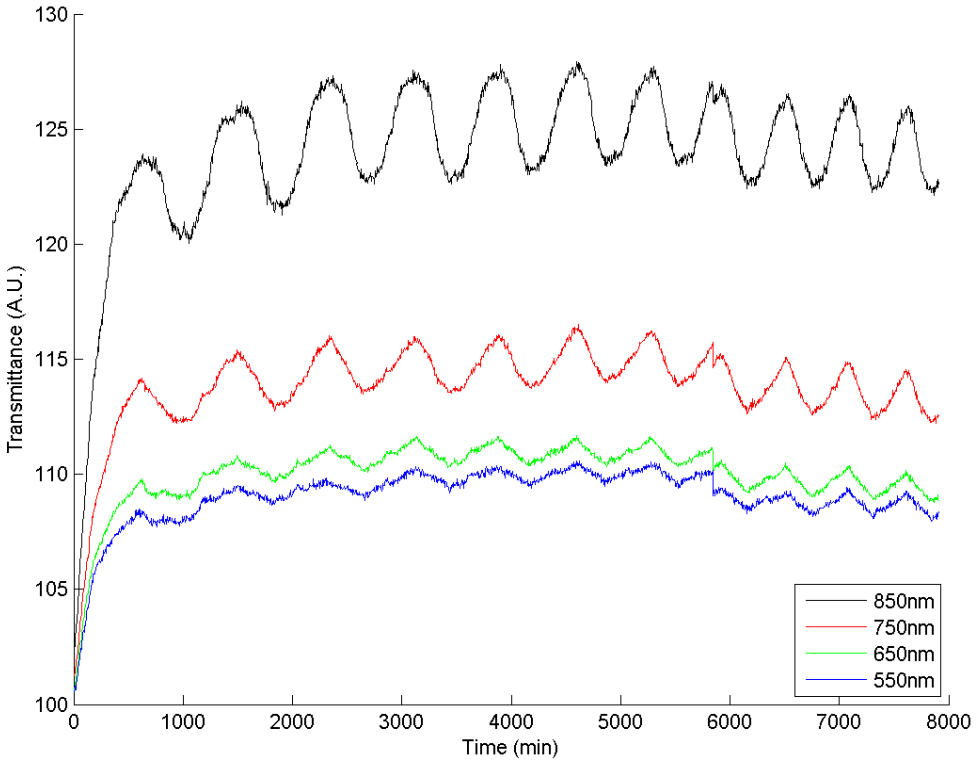


**Figure 17: Optical sensor transmittance vs. time at different wavelengths acquired over 11 charge and discharge cycles of a battery cell. The transmittance was measured with a spectrometer, which was calibrated such that the initial value was 100.**

## 5.7 Experimental Results

Experiments were carried out to establish the viability of the battery with embedded sensor. All of the following experiments were done with the OSI equipment described in Section 5.2. Several different sensors were fabricated and assembled into batteries. Some sensors were used more than once, however the batteries were not reusable and a new battery with fresh electrodes and electrolyte was assembled for each experiment. Figure 18 shows typical results that were obtained from three different cells using the same sensor. Approximately five cycles are shown for each cell, starting from a discharged state, with the transitions between charging and discharging indicated by vertical lines. The transmittance is shown as the amplified voltage output of the photodetector.

It can be seen in the results that the time for each cycle varies slightly among the cells, indicating that their capacity is not exactly the same. This is due to the battery assembly process, including slight differences in the size of the electrodes used in each battery, which were cut to size manually. There are also differences in the transmittance values, both in baseline and in the magnitude of the change, or delta, from the charged to discharged state. The delta varies from 60mV to 170mV and the baseline shifts by as much as 200mV for the cells shown. This can be attributed to differences in assembly where the pressure could not be precisely controlled and this would result in variation in optical contact between the fiber and electrode, affecting the magnitude of the transmittance.

Despite differences in the capacity and transmittance magnitude the sensor response is repeatable. The shape of the signal is generally the same among the different cells, with lower slope at the beginning and end of each charge and faster change in the middle. The discharge signal approximates the reverse of the charge signal, although some hysteresis is apparent. Experiments were carried out with different sensors and similar responses were seen with all sensors. Between different sensors the transmittance baseline may differ even more as the loss of optical power in the sensor is very sensitive to even small differences in the cladding thickness.

The experiments have shown that a consistent, repeatable response is achieved by the in-situ battery sensor. This signal can be used to estimate the SOC of the cell, as discussed in detail in the next chapter.

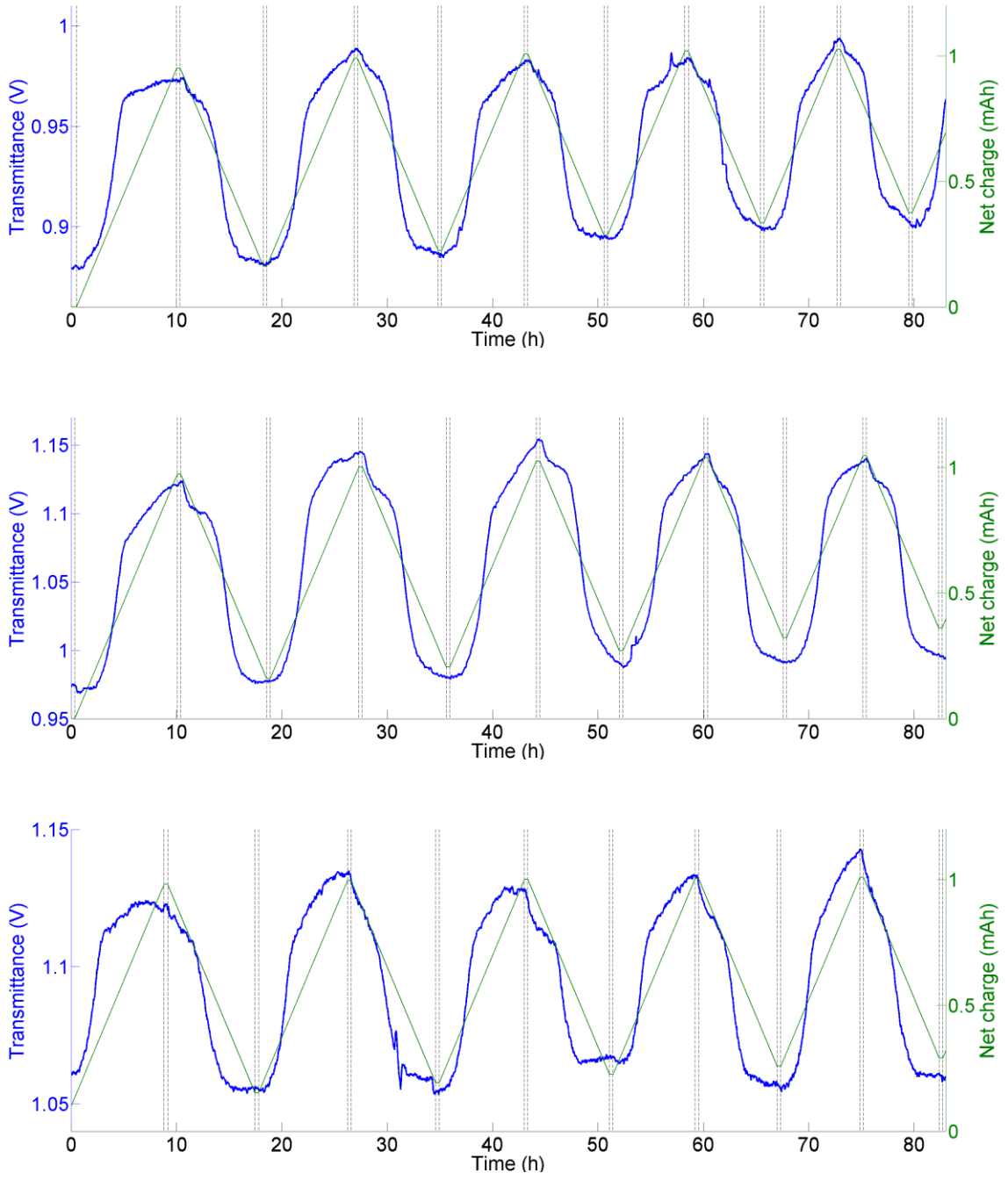


**Figure 18: Optical sensor transmittance over time and net charge over time from three different battery cells using the same sensor. Approximately five cycles are shown. The transmittance is the amplified output of a photodetector. The net charge is the integral of the battery current.**

# Chapter 6
# Determination of Sensor Characteristics

In this chapter results from several experiments described in Chapter 5 are presented. The sensor signal is post-processed in order to compensate for noise sources, and for differences between cells, such that data from different experiments can be compared. The characteristics of the sensor, including hysteresis, accuracy and sensitivity, are analyzed and discussed in terms of applicability to SOC estimation. Results are also compared with the theoretical model of a three layer stack of optical media presented in Section 4.4, and differences are examined and explained.

## 6.1 Post-processing of Optical Signal

### 6.1.1 High Frequency Noise

There are several sources of noise in the optical measurement system. Mainly, the noise comes from the electronic components and crosstalk between the circuits. This noise is high frequency and can be removed by filtering. A moving average filter, which acts as a low-pass filter, is used to smooth out the noise from the signal. Figure 19 shows the original signal overlaid with the smoothed signal. It can be seen that the smoothed signal follows the original very closely. Figure 20 shows a plot of the residuals of the smoothing, which is the difference between the original and smoothed signal. Ideally the residuals should be random and not show any trends. Here it can be seen that there are some patterns in the residuals, indicating that there is some distortion from the smoothing, however it is localized and does not affect the signal overall. In this case the high frequency noise can be removed from the signal fairly well in post-processing. For real time signal monitoring, it is preferable to eliminate the noise at the source by using higher quality electronics and an improved circuit design. This would be part of the future improvement of the sensor system.

### 6.1.2 Thermal noise

Temperature was found to have a significant effect on the optical signal. The two main sources of thermal noise are the electronics and the battery. The fiber itself also experiences slight changes in properties with temperature, due to the thermal coefficient of the refractive index of the materials. However, this is negligible when compared to the other thermal noise sources.

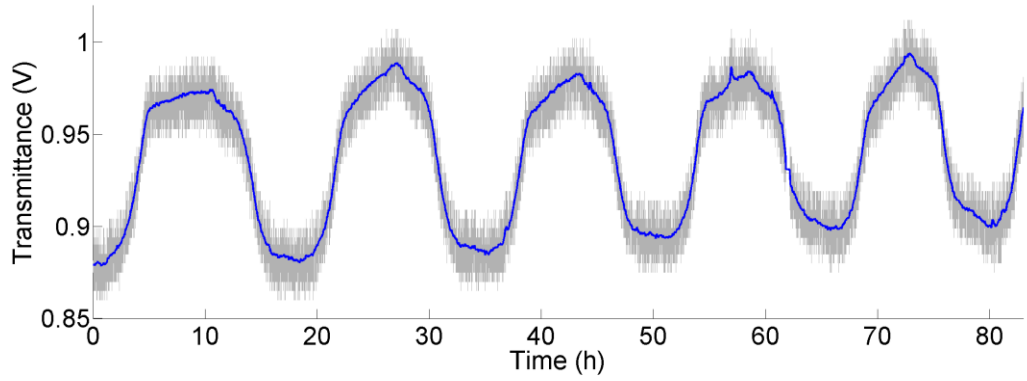


**Figure 19: Transmittance over time for a typical sensor signal showing the noisy raw signal in grey and the smoothed signal overlaid in black.**

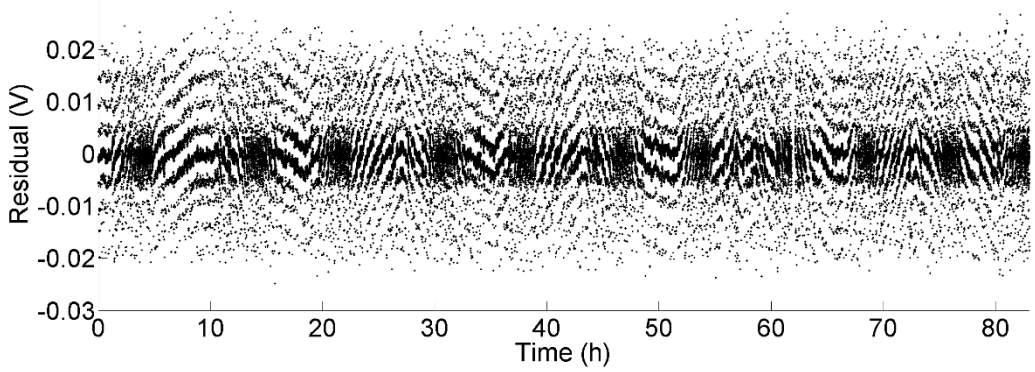


**Figure 20: Plot of the residuals, or the difference between raw and smoothed signal, from the smoothing shown in the previous figure.**

The main sources of thermal noise in the electronic signal acquisition system are the optical transmitter and receiver. Both devices show a dependence on temperature changes, with the output of the LED transmitter having a slightly larger thermal response than the receiver. The signal acquisition system does not include any compensation circuitry as this issue was not anticipated at the start, therefore compensation needed to be done in post-processing of the data.

Another source of thermal noise comes from the battery and it is both mechanical and chemical. The degree of the temperature effect varies between cells, where in some it is very slight and in others it is pronounced. One explanation for the former observation is that the contact between the fiber and the

electrode changes between cells. The battery in the Swagelok cell is compressed by two large steel cylinders and the amount of tightening and pressure could not be precisely controlled. The metal cylinders experience thermal expansion, which could change the pressure applied to the cell as the ambient temperature changes, thus changing the optical contact between sensor and electrode. This can have a significant effect on the amount of light that is absorbed by the electrode and subsequently on the output signal.

It was also observed that the degree of the temperature effect changes as the cell ages. This could be explained by the chemistry. During the first cycle a layer, called the solid-electrolyte interface (SEI) layer, is formed on the surface of the electrode and it continues changing over the life of the cell. The changes on the surface of the electrode affect the optical contact with the sensor and the optical signal. The aging of the cell is not consistent among the laboratory made batteries and this adds to the signal variations between cells.

All of the described thermal noise sources could not be eliminated before data acquisition and had to be dealt with in post-processing. A temperature compensation algorithm is used to reduce the temperature effects and is applied as follows. The battery is allowed to rest for 24 hours or more in order to obtain the temperature response without the effects of the battery cycling. Temperature sensors are used to record the temperature of the system. This data, along with the optical data obtained during the rest period, is used to determine the temperature compensation coefficients by finding a polynomial that best fits the optical data to the temperature in a least squares sense. For this fitting various degrees of polynomials were evaluated and a third degree polynomial was found to result in the best compensation results. The coefficients found by the fitting, and temperature data, are used to compensate the rest of the optical signal data.

Figure 21 shows an example of the signals during a typical rest period used in the temperature compensation. It can be seen that the raw sensor signal follows the change in temperature. The peak in the raw signal that coincides with the peak in the temperature is attenuated in the compensated signal. Ideally the compensated signal should be flat, but this is not the case here. Most notable is the dip around 14h where the temperature is decreasing and the algorithm overcompensates. The algorithm works reasonably well for gradual changes in temperature, but it does not handle sharp changes very well.

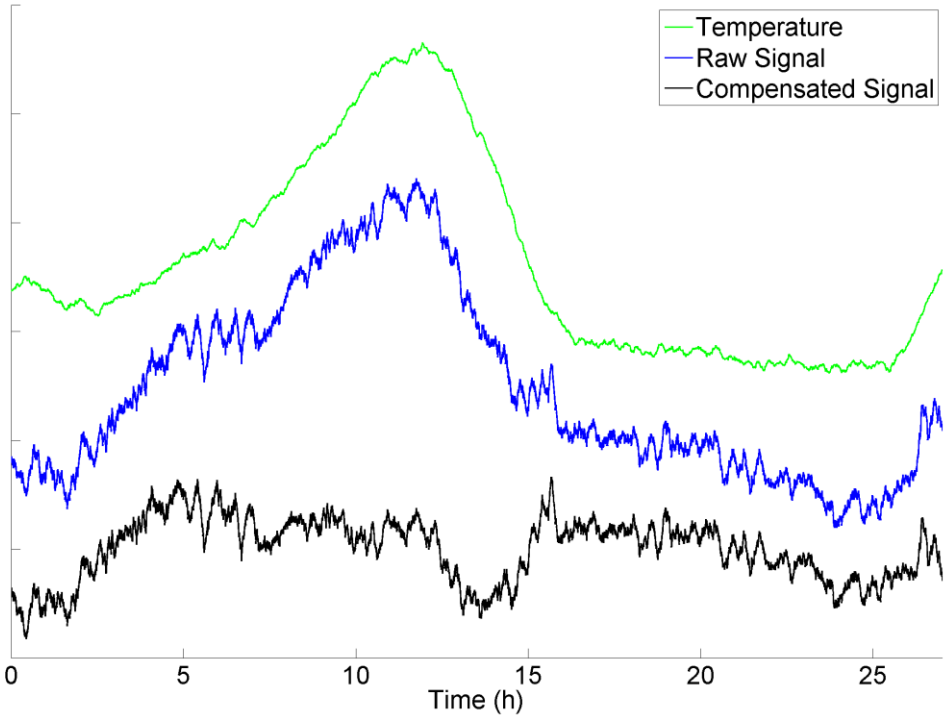


**Figure 21: Illustration of temperature compensation used in processing optical sensor signals. A typical rest period is shown with the temperature, raw and compensated signals.**

Given the available data it is not possible to completely remove the temperature effects in post-processing of the optical signals. These temperature effects should be eliminated at the source, which can be accomplished in several ways. The electronic signal acquisition circuit can be built to compensate for temperature effects on the optical components. A different battery structure, such as a pouch cell, a type used in many commercial batteries, would eliminate some of the mechanical effects. Commercial cells are also more stable and consistent in their performance, and it is expected that the temperature effects related to chemistry would be reduced in higher quality batteries.

### 6.1.3 Data Normalization

Given the data obtained with the setup used here it is necessary to perform further post-processing and normalization to allow for comparison among different cells. The data must be normalized both in terms of the SOC and to equalize the optical signal levels. For the purposes of this analysis the net

charge, or coulomb count, was used as a measure of the SOC of the battery. A full cycle from the lower voltage limit to the upper voltage limit (2.5V to 3.7V) was taken to represent the range of 0% to 100% SOC. The laboratory made batteries are not as stable as commercial cells and lose capacity with each cycle, therefore the net charge must be normalized in order to be more representative of the current SOC at each cycle.

The optical signal also requires normalization. The base level varies among different batteries, even when using the same sensor, due to differences in the optical contact that are a result of the assembly process. The signal is also subject to drift as the battery ages. The surface of the electrode changes as the SEI layer builds up on it and this affects the interaction between the sensor and the electrode, shifting the operating point of the sensor. The noise sources discussed in the previous section also distort the signal and cannot be fully compensated in some cases. The normalization of the transmittance adjusts for these distortions and provides a more accurate representation of the optical signal.

## 6.2 Sensor Signal Analysis

Data from several different cells was analyzed to determine the characteristics of the sensor. The normalization was performed by adjusting each individual charge and discharge curve such that the net charge is from 0 to 1 (0% to 100% SOC) and the endpoints of the transmittance are at 0 and 1.

Figures 22 to 24 show the normalized data for three different cells. The same sensor was used, hereafter referred to as Sensor #1, but the battery was reassembled with new electrodes for each cell. Cell #1, shown in Figure 22, was one of the more stable cells and the discharge curves are very close together. The charge curves are more divergent with the greatest differences in the middle of the cycle where the signal is changing quickly. Cell #2, shown in Figure 23, has greater differences and less consistency among both the charge and discharge curves. Cell #3, shown in Figure 24, is similar to Cell #2, but has a greater difference between the charge curves and the discharge curves.

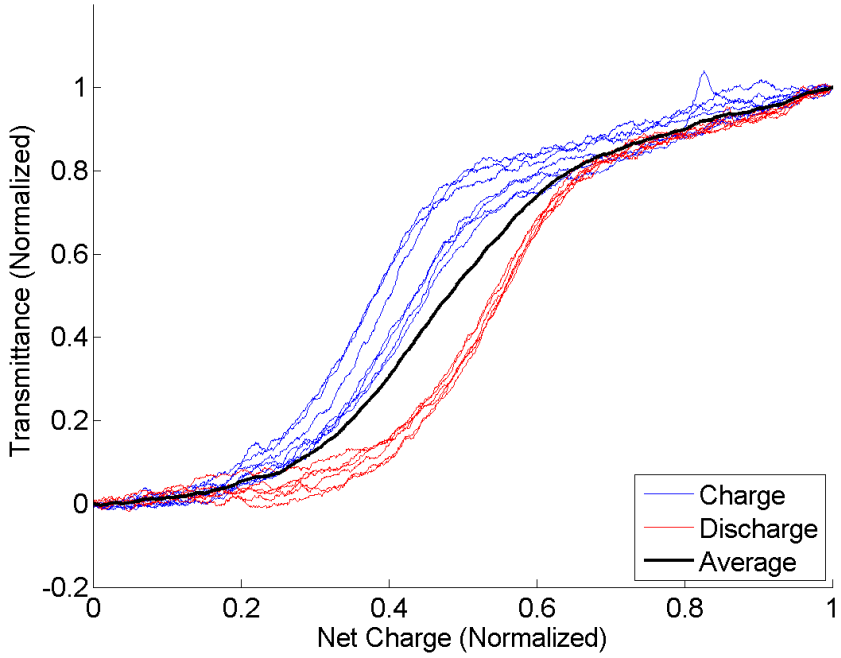


**Figure 22: Normalized transmittance vs. normalized net charge curves for several charge and discharge cycles obtained from Cell #1.**

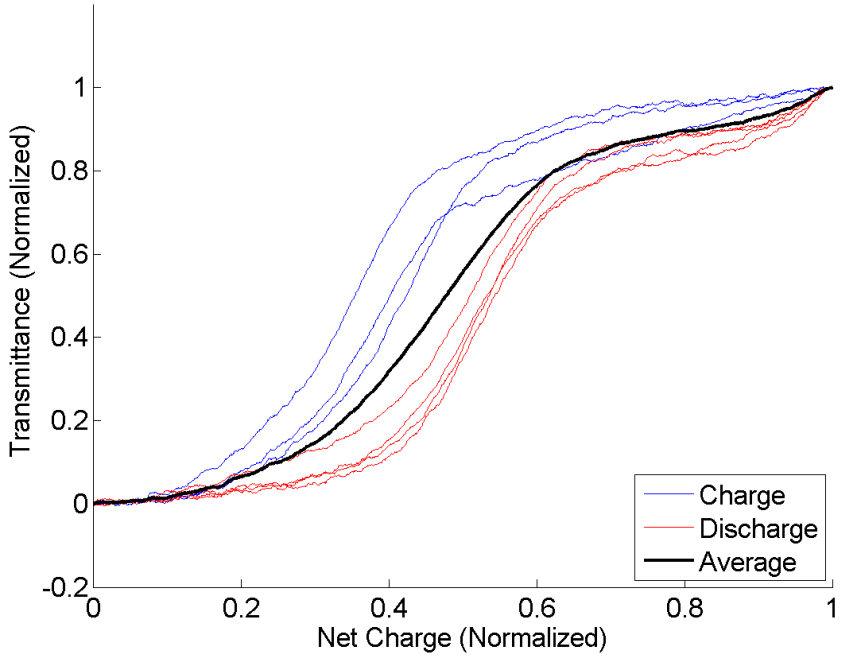


**Figure 23: Normalized transmittance vs. normalized net charge curves for several charge and discharge cycles obtained from Cell #2.**

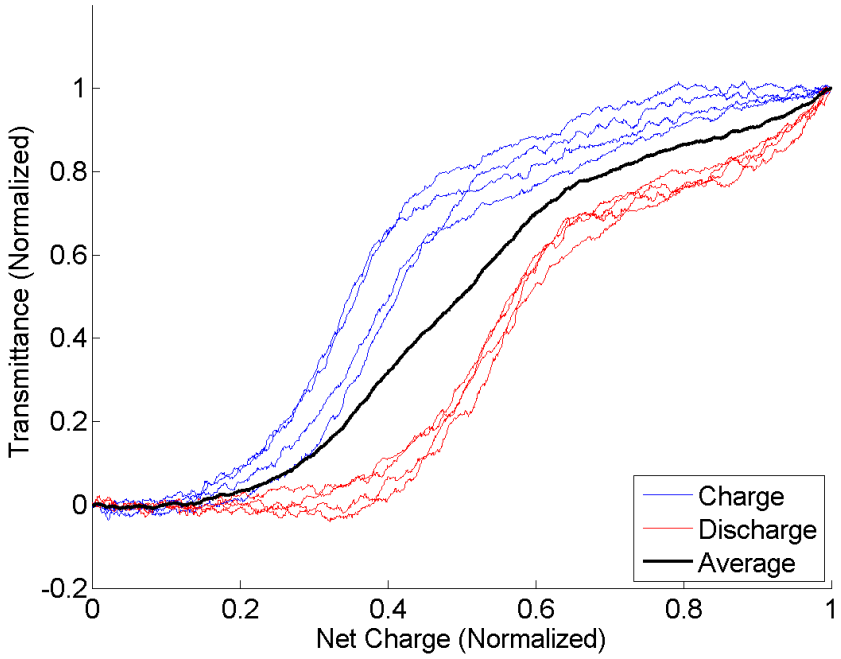


**Figure 24: Normalized transmittance vs. normalized net charge curves for several charge and discharge cycles obtained from Cell #3.**

These three cells (#1-3) have a very similar response as seen in the curve of the average of all charge and discharge curves. In all cases the curve has an 'S' shape with the signal being fairly flat up to about 30% SOC, then rising sharply up to about 60% SOC and with a low slope from about 60-100% SOC. These are the different operating regions of the sensor. The hysteresis, or difference between charge and discharge curves is very evident for all of these cells.

Further experiments were performed with different sensors. Figure 25 shows the normalized sensor signal data for Cell #4, which uses a different sensor than the previous three cells, referred to as Sensor #2. This sensor shows the same response as Sensor #1, with the same three operating regions from 0-30%, 30-60% and 60-100%. Cell #5, shown in Figure 26, uses Sensor #3. This cell has the least hysteresis and both the charge and discharge curves are very close to each other. The signal, once again, has the same response over the three operating regions. The results obtained from five different battery cells and three different sensors are all very similar and show the repeatability of the sensor response.

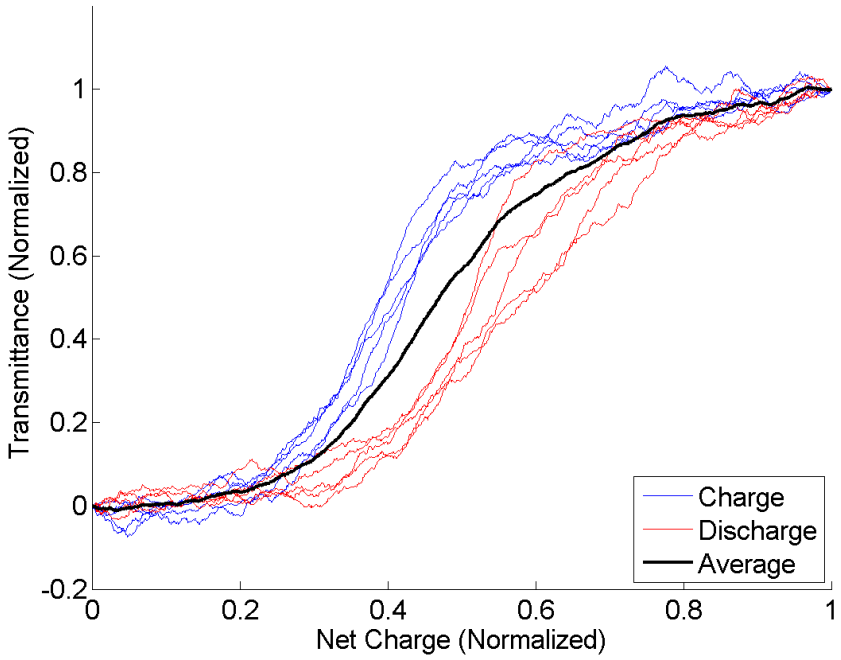


**Figure 25: Normalized transmittance vs. normalized net charge curves for several charge and discharge cycles obtained from Cell #4.**

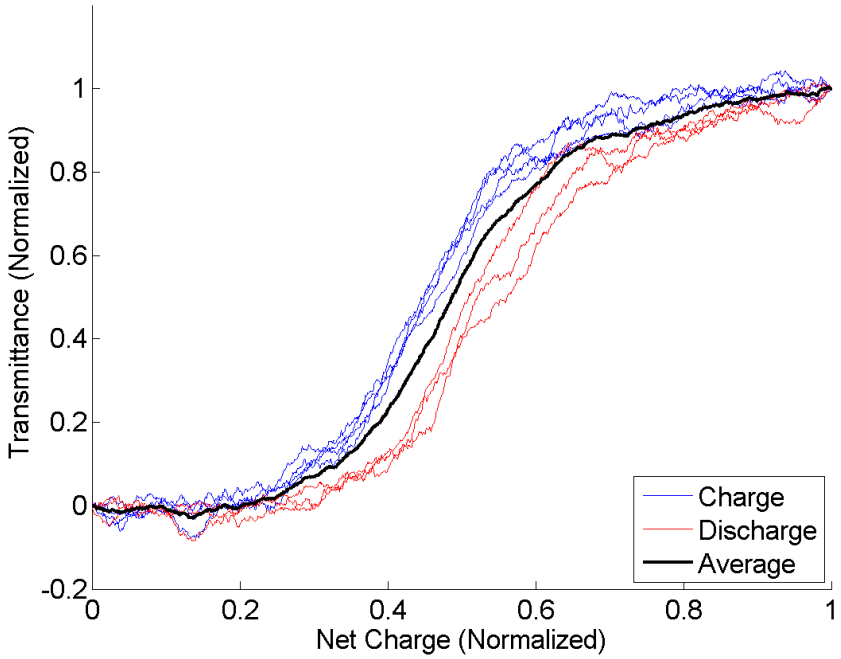


**Figure 26: Normalized transmittance vs. normalized net charge curves for several charge and discharge cycles obtained from Cell #5.**

### 6.2.1 Hysteresis

All of the cells studied exhibited some hysteresis. One of the differences among the cells is the degree of this hysteresis. This can be explained by the positioning of the sensor in the battery. The chemical reaction in the electrode does not affect the entire electrode at once, as was first discussed in Section 2.2. It begins near the current collector and proceeds through the electrode to the side in contact with the separator and sensor. This is illustrated in Figure 27. There may be variation in each cell in terms of the depth to which the sensor is embedded in the electrode. As the reaction progresses through the electrode it will affect the sensor at different points in time for different cells. The electrode is relatively thin and this difference would not be expected to be large, however it is reasonable to explain the observed shift of the operating region of about 5%.

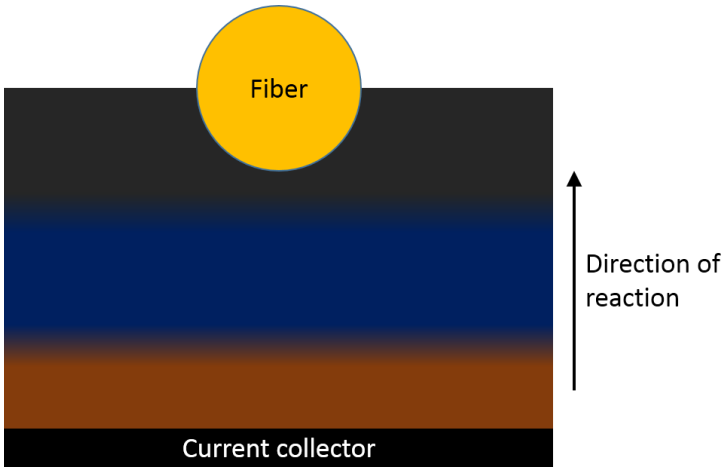


**Figure 27: Illustration of the progression of the lithiation reaction during charging in the graphite electrode. The colours shown for the lithiation stages are for illustration only and not true to the actual observed colours. The approximate position of the fiber sensor is shown.**

Some of the cells have quite high hysteresis, which can greatly reduce the accuracy of the sensor measurement. The hysteresis in the system can be reduced, as was seen in Cell #5, and possibly even eliminated. This can be achieved by more consistent battery fabrication and precise sensor placement. Assuming that the hysteresis cannot be eliminated at the source it can still be handled in applications where the battery does not switch from charging to discharging often by having a separate transfer function for charge and discharge. If done properly this could effectively eliminate hysteresis inaccuracies.

### 6.2.2 Accuracy

Accuracy, or more descriptively inaccuracy, is defined as the difference between the actual value and the measured value of a given quantity. For the purpose of estimating the sensor accuracy, the average of the optical signal for all the cycles is taken as the actual value of the signal. The sensor response is not linear and cannot be directly related to the SOC by a simple equation, therefore the average is used as the transfer function between the SOC and the transmittance signal.

The maximum absolute error for the five cells, calculated as the difference between each measured signal curve and the average of all curves, is summarized in Table 1. For Cells #1-3 it ranges from 30-36%, when all charge and discharge curves are taken into account. The hysteresis increases the error significantly as for the charge curves alone the error is 13-14% and for the discharge curves alone it is 5-8%. For Cells #4 and #5 the maximum absolute error ranges from 22-30%. The error for the charge curves alone is 6-10% and for discharge curves alone it is 9-19%. When the curves from all cells are plotted together and the combined average is used, the maximum absolute error is 37%.

The inaccuracy of 37% when considering several batteries together is quite high. This can be greatly reduced by improving several factors. The inaccuracies are much higher when comparing different cells. The can be mitigated by a calibration procedure that determines the transmission to SOC transfer function based on a set of cycles for each individual cell. This could be part of the manufacturing process and would not add great cost as each new cell undergoes several charging cycles as part of the fabrication process. The hysteresis also adds inaccuracy and if it was eliminated as discussed above, it would greatly improve the SOC estimate. When eliminating hysteresis and looking at each cell individually, the inaccuracy for the cells presented here is less than 14%. This is a reasonably good estimate and it could be improved further with more stable batteries and a better signal acquisition system.

**Table 1: Maximum absolute error for five different cells.**

| | **Cell #1** | **Cell #2** | **Cell #3** | **Cell #4** | **Cell #5** |
|---|---|---|---|---|---|
| **Charge only** | 13% | 14% | 13% | 10% | 6% |
| **Discharge only** | 5% | 8% | 7% | 19% | 9% |
| **Combined** | 30% | 36% | 36% | 30% | 22% |

### 6.2.3 Sensitivity

Sensitivity is an important characteristic of any sensor as it is part of the transfer function and defines the sensor response. Here, the sensitivity is defined as normalized transmittance units per % SOC (ntps). The response of this sensor can be divided into three regions: 0-30% SOC, 30-60% SOC, and 60-100% SOC. This is illustrated for a representative sensor response in Figure 28. The first and third regions have a low sensitivity and the signal change is relatively low. In the second region the response is relatively linear and has a high sensitivity. For Cells #1-3 that use Sensor #1 the sensitivity in this region is 2.1 ntps. For Cells #4 and #5 the sensitivity varies from 2.3 to 3.1 ntps. In the first region the sensitivity for Cells #1-3 is 0.41 ntps and for the other cells it varies from 0.2 to 0.36 ntps. In the third region it is slightly better than the first with 0.56 ntps for Cells #1-3 and 0.37 to 0.62 ntps for the other cells. The sensitivity for the five cells discussed here is summarized in Table 2.

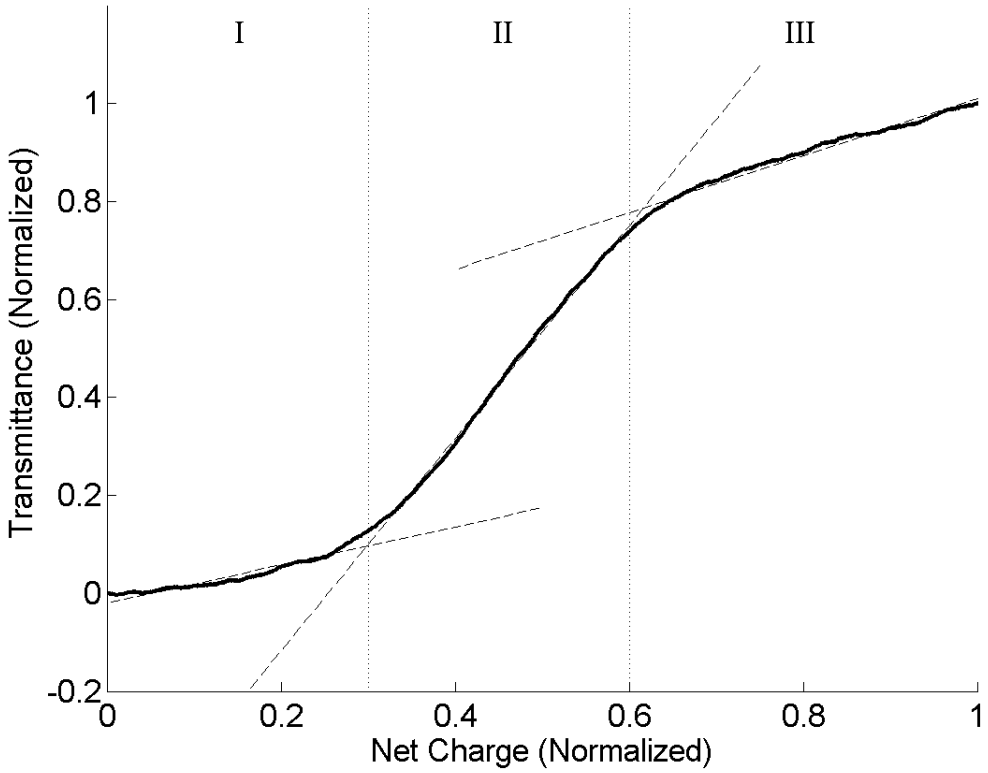


**Figure 28: Representative transmittance vs net charge curve showing the three regions of sensor operation.**

**Table 2: Sensitivity in the three regions of operation for five different cells in normalized transmittance units per % SOC.**

| | Cell #1 | Cell #2 | Cell #3 | Cell #4 | Cell #5 |
|---|---|---|---|---|---|
| **Region I** | 0.3882 | 0.4723 | 0.3699 | 0.3590 | 0.2041 |
| **Region II** | 2.1704 | 2.2051 | 1.9415 | 2.3188 | 2.6544 |
| **Region III** | 0.5815 | 0.4622 | 0.6374 | 0.6158 | 0.4941 |

The sensitivity of up to 2.65 in the central region of operation is very high compared to many sensors and it is expected that very good SOC estimates can be obtained in this region. The sensitivity in the first region is low, however this is not as much of a concern as it encompasses and small portion of the range and Li-ion batteries are generally kept outside of this range of SOC values as it can reduce battery life. The sensitivity in the third region is not very high, being on average 0.56 for the five cells studied. It is possible to achieve high accuracy even at this sensitivity, but it may be possible to increase the sensitivity in the third region by exciting the sensor at a different wavelength. It was seen previously in Section 5.6 that the sensor response varies at different wavelengths and it is possible that a wavelength that has not yet been studied will produce a more sensitive response in all regions. This is an important path for future study of the sensor.

### 6.2.4 Partial cycling

Partial charge and discharge cycles were performed to determine the sensor response when the battery is not fully charged or discharged. Figure 29 shows plots of partial cycling for two different batteries with different sensors. Curves are shown for four different ranges of SOC, including a full cycle. The ranges used were 0-100% SOC for the full cycle, 10-90% for Cycle 2, 20-80% for Cycle 3, and 30-70% for Cycle 4. The full cycle curve is used to normalize the other curves in terms of both net charge and transmittance. Each curve is scaled by the same factor, which is the one that normalizes the full cycle curve. The partial cycle curves have also been shifted such that they coincide with the full cycle curve at the central SOC value of 50%.

The partial cycle curves fit very well with the full cycle curves. The shape varies slightly at the beginning and end of the cycles, most notable in Cycles 3 and 4 for the charge curves of both cells, which can be explained by the progression of the lithiation reaction through the electrode, discussed

previously. Other than these small discrepancies, the partial cycles have the same shape and slope as the full cycle. The hysteresis is also noticeable in these plots, as the partial discharges do not lie in the same position along the full cycle curve as the partial charges.

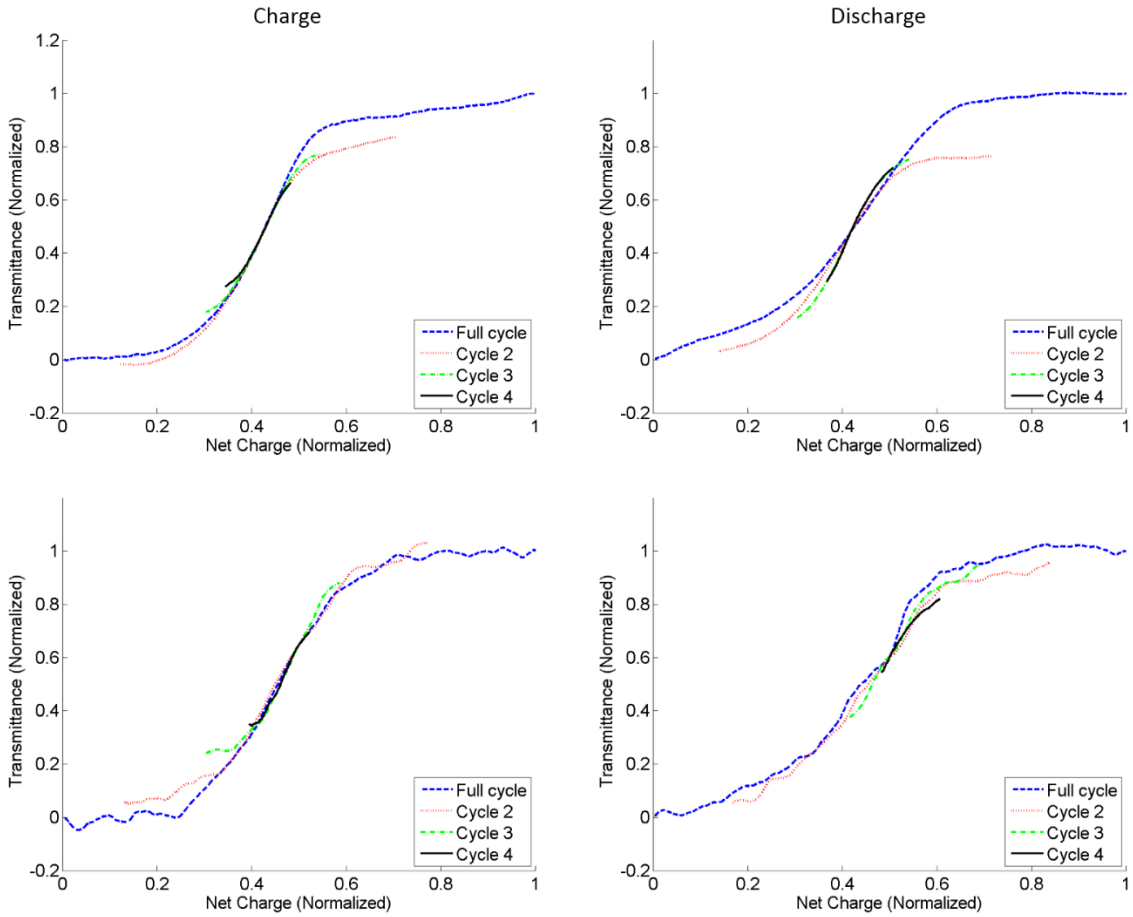


**Figure 29: Normalized transmittance vs. normalized net charge curves for partial cycles obtained from two different battery cells (top and bottom). Charge cycles are on the left and discharge cycles on the right. One curve from each of four ranges of SOC is shown. The range for Cycle 2 is 10-90%, for Cycle 3 it is 20-80%, for Cycle4 it is 30-70%.**

The partial cycling shows that the shape and slope of the transmission curve is consistent even when the battery is charged between intermediate SOC values. This shows that the sensor can track the SOC without requiring recalibration points, assuming that the initial calibration is correct. Long term studies with more stable batteries would need to be done to determine if there is drift in the optical

signal over time that may happen due to changes in the SEI layer. For commercial batteries this would be a very slow change and could be accounted for by recalibration cycles that would be required only between long periods of operation.

## 6.3 Comparison with Theory

The transfer matrix model described in Chapter 4 can be used to relate the changes in transmission of the sensor to the optical properties of the electrodes. The transmission is related to the SOC as shown above, and it is also related to a set of refractive index values. By combining these relationships it may be possible to establish a relation between the SOC and refractive index of the electrodes. This is not straightforward and is complicated by several factors that affect the sensor response, such as surface roughness of the electrode, electrolyte composition and the migration of the lithiation reaction.

Based on the literature it was predicted in Section 4.5 that the optical response of the sensor may be related to the stages of lithiation of the electrode. The stages of lithiation can be seen in the voltage profile of a cycling cell. The voltage experiences more pronounced changes in slope at the stage transitions as has been demonstrated with half cells [46]. Half cells are composed of a Li metal electrode paired with either the graphite anode or Li-ion cathode of a full cell. An experiment was conducted to determine if the voltage profile can be related to the lithiation stage transitions in a full cell. A half cell was prepared using the same materials as the full cells used for the experiments presented so far, with the only difference being that the LiFePO4 cathode is replaced by a lithium metal electrode of the same size. Figure 30 shows the voltage profiles of this half cell and a full cell for a single charge. (The voltage of a half cell decreases during charge, as opposed to the full cell, which increases). Vertical lines denote the points in the half cell voltage profile where the slope changes. These point coincide with slope changes in the voltage profile of the full cell. By extension, the transition points for the graphite lithiation stages can be determined from the voltage profile of the cells used for sensor testing.

Figure 31 shows the optical signal compared to the voltage profile with the voltage transitions marked for a single charge. The transitions in the voltage coincide with changes in the slope of the optical signal. Based on the voltage there are four stages, which correspond with the regions of operation of the sensor when the first two stages are taken together. Each of the graphite lithiation stages has

distinct optical properties and there are relatively sharp boundaries between them, as discussed in Section 4.5. The optical properties of the stages can be related to the changes in slope in the regions of the optical signal.

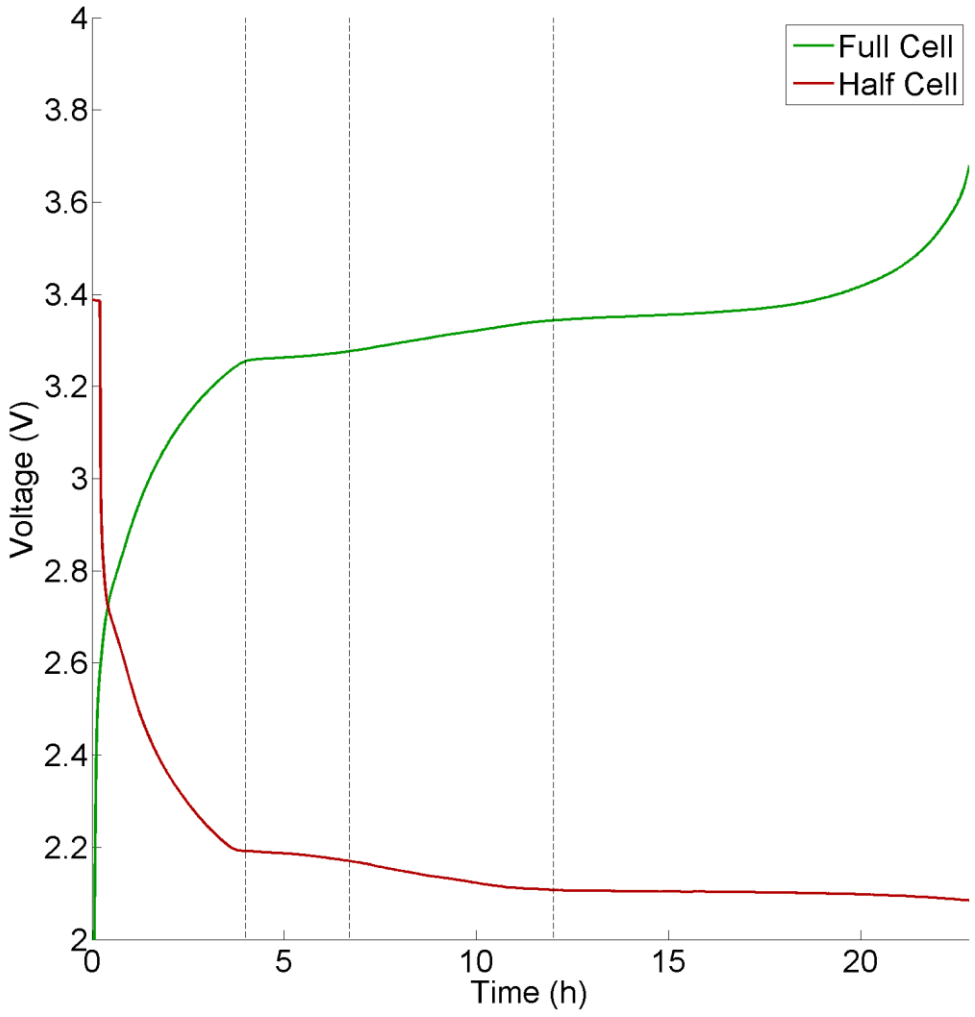


**Figure 30: Comparison of voltage profiles of a half cell and a full cell for a single charge with the voltage transitions marked.**

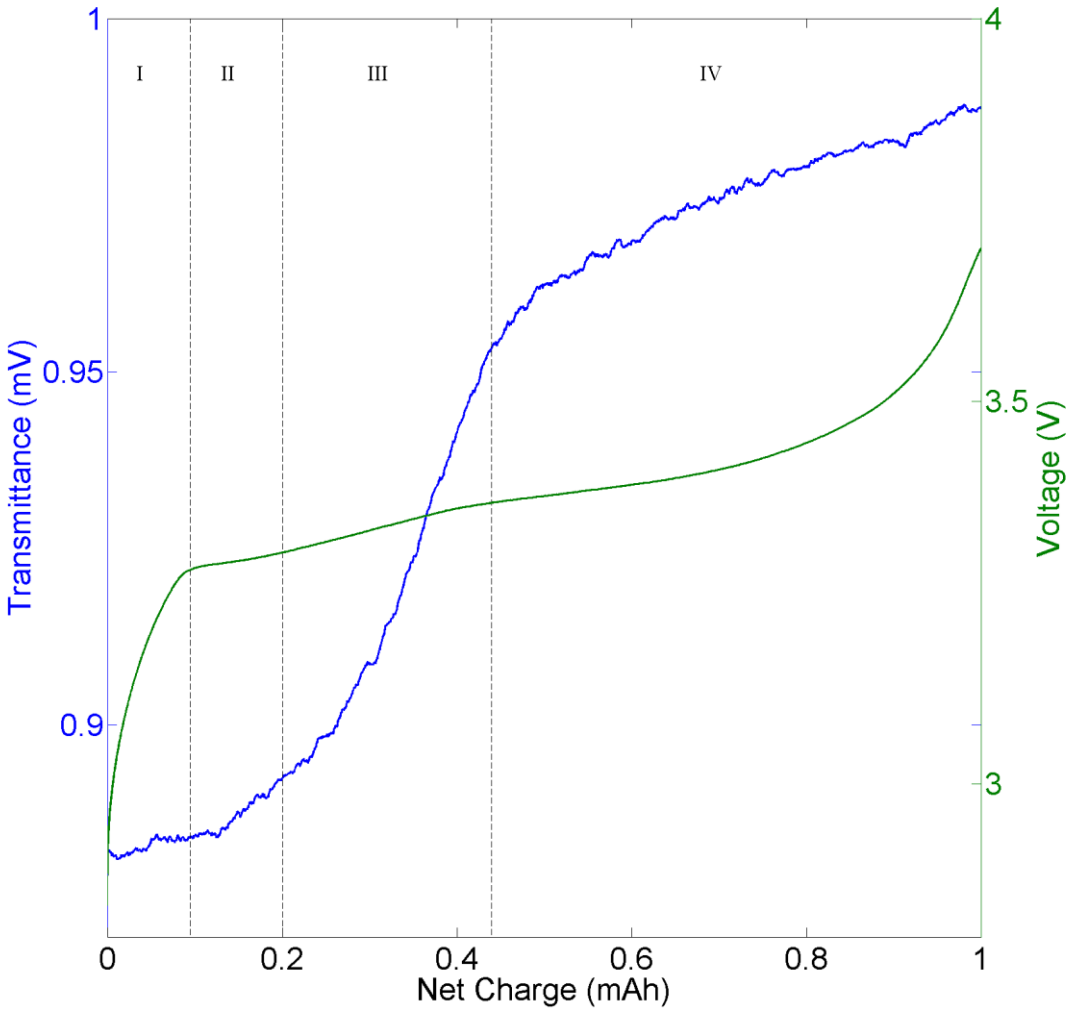


**Figure 31: Comparison of typical optical signal and voltage profile for a single charge with voltage transitions marked.**

Each transmittance value is associated with one or more sets of values for the refractive index and extinction coefficient. The real part of the refractive index of graphite is around n=3. At these values of the real refractive index the extinction coefficient dominates the transmittance. Therefore, the part of the transmission change that is due to optical changes is likely due to the extinction coefficient. From Figure 9, a change in k of 0.5 results in about 2% change in transmittance at n=3. In the

experiments conducted with live batteries the transmittance varied by more than 5%. This implies that there are other factors, besides the optical refractive index changes, that are affecting the transmission.

There are several factors that may affect the transmission. These include the electrolyte composition, surface contact between the sensor and electrode, and the migration of the lithiation reaction. The electrolyte has contact with the sensing region in the spaces where there is no contact with the electrode. The refractive index of the electrolyte is estimated to be less than the index of the cladding, which means it should not affect the transmittance, assuming its extinction coefficient is zero. To verify this assumption, an experiment was carried out, using the same setup described in Section 5.4, with the exception that the sensor was placed between two layers of separator. The sensor was not in contact with either electrode, but had contact with the electrolyte. In this experiment a very slight variation related to the cycling of the cell was seen in the signal. This shows that the electrolyte may have a marginal effect on the transmittance. This could be due to inhomogeneity caused by the change in concentration of lithium ions in the electrolyte, or it could indicate that the extinction coefficient of the electrolyte is not zero. Further study of the sensor response with different concentrations of electrolyte is required to determine its effect on the sensor.

The surface of the electrode changes with the various reactions happening in the cell and this affects the contact between the sensor and electrode. As the electrode is lithiated the makeup of the particles on the surface changes. The surface could become rougher or smoother and this affects the amount of contact with the sensor. There is also a volume change that occurs in the cell during charging and discharging. This volume change could lead to pressure changes inside the cell, which changes the amount of contact with the sensor. The surface contact change may be the greatest influence on the transmission change and requires further study to determine its precise effect.

The migration of the lithiation reaction through the electrode could also play a role in the shape of the signal as it will not uniformly affect the entire area of the sensor at once. The kinetics of this reaction are not well known. The electrode is relatively thin, and it may be that the reaction migrates quickly enough that the time it takes to cover the entire sensor surface is not significant when compared to the overall charge and discharge time. A planar optical waveguide, a possible realization for the sensor, would eliminate the effect of the migration kinetics and is one avenue for further study.

# Chapter 7
# Conclusions and Future Work

## 7.1 Conclusions

In this thesis a sensor was developed that is capable of monitoring the SOC of Li-ion batteries. The sensor is fabricated by etching a fiber optic to thin the cladding such that the guided light in the core interacts with the external medium of the battery electrode. Multimode silica fiber optics were selected for the sensor. Multimode fibers are sufficiently small to fit inside the battery without interfering with its performance, while being easier to handle and allowing for simpler coupling of light, which reduces cost. Silica does not react with the battery chemicals, meaning that the sensor can withstand the in-situ environment and not interfere with the chemistry. The sensor is inserted into a functional prototype battery prepared in a Swagelok® cell.

The sensor is excited by an LED source at 850nm and the output signal is monitored as the battery is charged and discharged. The wavelength was selected based on previous studies and experiments carried out with the in-situ sensor. The sensor signal is based on intensity modulation of the light guided by the fiber. This is one of the simplest methods both in terms of fabrication of the sensor and in terms of interrogating the output signal, which allows for a very low cost system.

Based on several experiments the sensor output follows the charging a discharging of the battery very closely with a consistent pattern. The sensor response is repeatable with different sensors and battery cells. The sensor has a high sensitivity in the region of 30-60% SOC and a good sensitivity in the other regions. An accuracy of 14% can be achieved with the current system when the sensor output is normalized for each individual cell and the charge and discharge cycles are considered separately.

The battery sensor system can be improved to achieve better SOC estimation accuracy. The acquisition system used here had issues with temperature effects and other sources of noise. These can be addressed in the design of the circuits of the system, thus removing the need for much of the post-processing and resulting in a cleaner signal. More stable batteries would result in a more repeatable sensor output, which is expected to increase the accuracy of the SOC measurement.

## 7.2 Contributions

### 7.2.1 Insertion of Fiber Optic Sensor into Battery

The main novelty of this sensor is that is can be used to monitor the internal state of a battery. It is located inside the battery in contact with the anode electrode. The sensor does not interfere with the performance of the battery and it can withstand the internal chemical environment and remain functional.

### 7.2.2 SOC Estimation Based on Direct Measurements of Battery Environment

The sensor is capable of monitoring the internal environment of the battery in real time. The sensor output is a direct representation of the immediate internal state of the battery. This allows it to follow the SOC closely. Very little additional computation is required to obtain the SOC estimate from the sensor output.

### 7.2.3 Low Cost of Sensor System

The signal acquisition system uses basic components that are inexpensive, especially when manufactured in bulk. The system uses a single wavelength light source, which can be an LED or laser transmitter, and a basic photodetector with an amplifier. The photodetector output voltage is read directly and processed in software. The processing does not require high computational capacity.

## 7.3 Future Work

### 7.3.1 Sensor Design and Fabrication

Further study is needed to optimize the sensor and its response. The cladding thickness had a significant effect on the sensitivity of the sensor. A more consistent and precise fabrication procedure would allow for finer control and optimization of the sensitivity. Batch fabrication would make sensors that are more similar and require less calibration. The testing procedure could also be improved to ensure that each sensor meets the specification more closely.

Further study is needed on the sensor response at different wavelengths. The studies mentioned in this thesis have not considered wavelengths below 400nm and above 900nm. It is possible that a higher

sensitivity can be achieved at different wavelengths, especially for the regions where the current wavelength does not show high sensitivity.

### 7.3.2 Signal Acquisition System

The signal acquisition system can be improved to reduce the noise and to avoid temperature effects so that they don't have to be removed in post-processing. This can be done by adding reference circuits and better gain amplifiers with reduced noise.

### 7.3.3 Battery Consistency and Sensor Placement

With the prototype batteries used here there are large differences in the sensor response between cells. Studies need to be done with commercial grade batteries to get a more accurate view of the sensor performance. This would also ease the development of the calibration procedure that adjusts SOC estimation parameters for each individual cell.

The placement of the sensor needs to be addressed. If the sensor is fully embedded in the anode it would likely produce a stronger signal and it would be more consistent from one cell to another. This would have to be done during fabrication of the battery electrode. The location of the sensor in the battery should also be studied further. For larger batteries there may be differing responses in different locations, such as closer to or further from the battery terminals. For batteries consisting of multiple layers of electrodes the consistency of responses of sensors placed between different layers could also be studied.

# References


[1] S. Piller, M. Perrin, and A. Jossen, “Methods for state-of-charge determination and their applications,” *J. Power Sources*, vol. 96, no. 1, pp. 113–120, Jun. 2001.

[2] K. S. Ng, C.-S. Moo, Y.-P. Chen, and Y.-C. Hsieh, “Enhanced coulomb counting method for estimating state-of-charge and state-of-health of lithium-ion batteries,” *Appl. Energy*, vol. 86, no. 9, pp. 1506–1511, Sep. 2009.

[3] W.-Y. Chang, “The State of Charge Estimating Methods for Battery: A Review,” *ISRN Appl. Math.*, vol. 2013, p. e953792, Jul. 2013.

[4] T. Kim, W. Qiao, and L. Qu, “Real-time state of charge and electrical impedance estimation for lithium-ion batteries based on a hybrid battery model,” in *2013 Twenty-Eighth Annual IEEE Applied Power Electronics Conference and Exposition (APEC)*, 2013, pp. 563–568.

[5] S. Lee, J. Kim, J. Lee, and B. H. Cho, “State-of-charge and capacity estimation of lithium-ion battery using a new open-circuit voltage versus state-of-charge,” *J. Power Sources*, vol. 185, no. 2, pp. 1367–1373, Dec. 2008.

[6] M. A. Roscher and D. U. Sauer, “Dynamic electric behavior and open-circuit-voltage modeling of LiFePO4-based lithium ion secondary batteries,” *J. Power Sources*, vol. 196, no. 1, pp. 331–336, Jan. 2011.

[7] S. Rodrigues, N. Munichandraiah, and A. K. Shukla, “AC impedance and state-of-charge analysis of a sealed lithium-ion rechargeable battery,” *J. Solid State Electrochem.*, vol. 3, no. 7–8, pp. 397–405, Sep. 1999.

[8] L. Ran, W. Junfeng, W. Haiying, and L. Gechen, “Prediction of state of charge of Lithium-ion rechargeable battery with electrochemical impedance spectroscopy theory,” in *2010 the 5th IEEE Conference on Industrial Electronics and Applications (ICIEA)*, 2010, pp. 684–688.

[9] F. Huet, “A review of impedance measurements for determination of the state-of-charge or state-of-health of secondary batteries,” *J. Power Sources*, vol. 70, no. 1, pp. 59–69, Jan. 1998.

[10] H. Blanke, O. Bohlen, S. Buller, R. W. De Doncker, B. Fricke, A. Hammouche, D. Linzen, M. Thele, and D. U. Sauer, “Impedance measurements on lead–acid batteries for state-of-charge, state-of-health and cranking capability prognosis in electric and hybrid electric vehicles,” *J. Power Sources*, vol. 144, no. 2, pp. 418–425, Jun. 2005.

[11] G. L. Plett, “Extended Kalman filtering for battery management systems of LiPB-based HEV battery packs: Part 3. State and parameter estimation,” *J. Power Sources*, vol. 134, no. 2, pp. 277–292, Aug. 2004.

[12] J. Lee, O. Nam, and B. H. Cho, “Li-ion battery SOC estimation method based on the

reduced order extended Kalman filtering," *J. Power Sources*, vol. 174, no. 1, pp. 9–15, Nov. 2007.

[13] D. Di Domenico, G. Fiengo, and A. Stefanopoulou, "Lithium-ion battery state of charge estimation with a Kalman Filter based on a electrochemical model," in *IEEE International Conference on Control Applications, 2008. CCA 2008*, 2008, pp. 702–707.

[14] H. He, R. Xiong, X. Zhang, F. Sun, and J. Fan, "State-of-Charge Estimation of the Lithium-Ion Battery Using an Adaptive Extended Kalman Filter Based on an Improved Thevenin Model," *IEEE Trans. Veh. Technol.*, vol. 60, no. 4, pp. 1461–1469, May 2011.

[15] F. Sun, X. Hu, Y. Zou, and S. Li, "Adaptive unscented Kalman filtering for state of charge estimation of a lithium-ion battery for electric vehicles," *Energy*, vol. 36, no. 5, pp. 3531–3540, May 2011.

[16] W. X. Shen, C. C. Chan, E. W. C. Lo, and K. T. Chau, "A new battery available capacity indicator for electric vehicles using neural network," *Energy Convers. Manag.*, vol. 43, no. 6, pp. 817–826, Apr. 2002.

[17] A. Affanni, A. Bellini, C. Concari, G. Franceschini, E. Lorenzani, and C. Tassoni, "EV battery state of charge: neural network based estimation," in *Electric Machines and Drives Conference, 2003. IEMDC'03. IEEE International*, 2003, vol. 2, pp. 684–688 vol.2.

[18] A. J. Salkind, C. Fennie, P. Singh, T. Atwater, and D. E. Reisner, "Determination of state-of-charge and state-of-health of batteries by fuzzy logic methodology," *J. Power Sources*, vol. 80, no. 1–2, pp. 293–300, Jul. 1999.

[19] M. Charkhgard and M. Farrokhi, "State-of-Charge Estimation for Lithium-Ion Batteries Using Neural Networks and EKF," *IEEE Trans. Ind. Electron.*, vol. 57, no. 12, pp. 4178–4187, Dec. 2010.

[20] Y. Shen, "Adaptive online state-of-charge determination based on neuro-controller and neural network," *Energy Convers. Manag.*, vol. 51, no. 5, pp. 1093–1098, May 2010.

[21] A. M. Cao-Paz, J. Marcos-Acevedo, A. Del Río-Vázquez, C. Martínez-Peñalver, A. Lago-Ferreiro, A. A. Nogueiras-Meléndez, and J. Doval-Gandoy, "A Multi-Point Sensor Based on Optical Fiber for the Measurement of Electrolyte Density in Lead-Acid Batteries," *Sensors*, vol. 10, no. 4, pp. 2587–2608, Mar. 2010.

[22] G. P. Hancke, "A fibre-optic density sensor for monitoring the state-of-charge of a lead-acid battery," in *, 6th IEEE Instrumentation and Measurement Technology Conference, 1989. IMTC-89. Conference Record*, 1989, pp. 486–489.

[23] A. Raghavan, P. Kiesel, and B. Saha, "Monitoring and management for energy storage devices," US20140092375 A1, 03-Apr-2014.

[24] S. Basu, C. Zeller, P. J. Flanders, C. D. Fuerst, W. D. Johnson, and J. E. Fischer, "Synthesis and properties of lithium-graphite intercalation compounds," *Mater. Sci. Eng.*, vol. 38, no. 3, pp. 275–283, Jun. 1979.

[25] P. Pfluger, K.-P. Ackermann, R. Lapka, E. Schüpfer, R. Jeker, H.-J. Güntherodt, E. Cartier, and F. Heinrich, "Concentration dependence of optical reflectivity and 2γ-angular correlation distribution of positron annihilation in donor- and acceptor-intercalated graphite," *Synth. Met.*, vol. 2, no. 3–4, pp. 285–293, Dec. 1980.

[26] J. E. Fischer, J. M. Bloch, C. C. Shieh, M. E. Preil, and K. Jelley, "Reflectivity spectra and dielectric function of stage-1 donor intercalation compounds of graphite," *Phys. Rev. B*, vol. 31, no. 8, pp. 4773–4783, Apr. 1985.

[27] L. Xie and J. Lu, "In situ UV–Vis diffuse reflectance studies on lithium-intercalated carbons," *J. Electroanal. Chem.*, vol. 497, no. 1–2, pp. 159–162, Feb. 2001.

[28] S. J. Harris, A. Timmons, D. R. Baker, and C. Monroe, "Direct in situ measurements of Li transport in Li-ion battery negative electrodes," *Chem. Phys. Lett.*, vol. 485, no. 4–6, pp. 265–274, Jan. 2010.

[29] P. Maire, H. Kaiser, W. Scheifele, and P. Novák, "Colorimetric determination of lithium-ion mobility in graphite composite electrodes," *J. Electroanal. Chem.*, vol. 644, no. 2, pp. 127–131, Jun. 2010.

[30] P. Maire, A. Evans, H. Kaiser, W. Scheifele, and P. Novák, "Colorimetric Determination of Lithium Content in Electrodes of Lithium-Ion Batteries," *J. Electrochem. Soc.*, vol. 155, no. 11, pp. A862–A865, Nov. 2008.

[31] R. C. Norris, "Spectroscopy of Lithium Iron Phosphate Battery Electrodes," Univ. of Waterloo, Waterloo, ON, R003-2012, 2012.

[32] S. M. Chandani, "Fibre optic sensors based on D-shaped elliptical core fibres," *PhD Thesis*, p. 191, 2007.

[33] A. Gaston, I. Lozano, F. Perez, F. Auza, and J. Sevilla, "Evanescent wave optical-fiber sensing (temperature, relative humidity, and pH sensors)," *IEEE Sens. J.*, vol. 3, no. 6, pp. 806–811, Dec. 2003.

[34] L. Bilro, N. Alberto, J. L. Pinto, and R. N. Nogueira, "A simple and low-cost cure monitoring system based on a side-polished plastic optical fibre," *Meas. Sci. Technol.*, vol. 21, no. 11, p. 117001, Nov. 2010.

[35] D. Jose, "An optical fibre based evanescent wave sensor to monitor the deposition rate of thin films," *Thin Solid Films*, vol. 325, pp. 264–267, Jul. 1998.

[36] N. J. Harrick, *Internal Reflection Spectroscopy*. John Wiley & Sons, Inc., 1967.

[37] S. Ekgasit and A. Padermshoke, "Optical Contact in ATR/FT-IR Spectroscopy," *Appl. Spectrosc.*, vol. 55, no. 10, pp. 1352–1359, Oct. 2001.

[38] B. Lee, "Review of the present status of optical fiber sensors," *Opt. Fiber Technol.*, vol. 9, no. 2, pp. 57–79, Apr. 2003.

[39] E. Udd, "An overview of fiber-optic sensors," *Rev. Sci. Instrum.*, vol. 66, no. 8, pp.

4015–4030, Aug. 1995.

[40] A. C. Garcia and J. E. Cuena, “Transduction Techniques based on Intensity Modulation of Light,” in *Handbook of Optical Fibre Sensing Technology*, John Wiley & Sons Ltd., 2002, pp. 221–233.

[41] S.-M. Tseng and C.-L. Chen, “Side-polished fibers,” *Appl. Opt.*, vol. 31, no. 18, pp. 3438–3447, Jun. 1992.

[42] E. Hecht, *Optics*, 4 edition. Reading, Mass: Addison-Wesley, 2001.

[43] V. Ruddy, B. D. MacCraith, and J. A. Murphy, “Evanescent wave absorption spectroscopy using multimode fibers,” *J. Appl. Phys.*, vol. 67, no. 10, pp. 6070–6074, May 1990.

[44] H. A. Macleod, *Thin-Film Optical Filters, Third Edition*. CRC Press, 2001.

[45] J. Rheims, J. Köser, and T. Wriedt, “Refractive-index measurements in the near-IR using an Abbe refractometer,” *Meas. Sci. Technol.*, vol. 8, no. 6, p. 601, Jun. 1997.

[46] T. Ohzuku, Y. Iwakoshi, and K. Sawai, “Formation of Lithium-Graphite Intercalation Compounds in Nonaqueous Electrolytes and Their Application as a Negative Electrode for a Lithium Ion (Shuttlecock) Cell,” *J. Electrochem. Soc.*, vol. 140, no. 9, pp. 2490–2498, Sep. 1993.

# Appendix A
# Reflectance of a Thin Film

A thin film with incident plane wave is illustrated in Figure 8. Here, waves in the direction of incidence will be denoted with the symbol + (positive-going wave) and waves in the opposite direction with the symbol – (negative-going wave). The boundary between the incident medium and the thin film is denoted by a, and the boundary between the thin film and the third medium is denoted by b. At boundary b the tangential components of the electric and magnetic fields are:

$$\boldsymbol{E}_b = \boldsymbol{E}_{1b}^{+} + \boldsymbol{E}_{1b}^{-}$$
$$\boldsymbol{H}_b = \eta_1 \boldsymbol{H}_{1b}^{+} - \eta_1 \boldsymbol{H}_{1b}^{-}$$

$$\boldsymbol{E}_{1b}^{+} = \frac{1}{2}\left(\frac{\boldsymbol{H}_b}{\eta_1} + \boldsymbol{E}_b\right)$$
$$\boldsymbol{E}_{1b}^{-} = \frac{1}{2}\left(-\frac{\boldsymbol{H}_b}{\eta_1} + \boldsymbol{E}_b\right)$$
$$\boldsymbol{H}_{1b}^{+} = \eta_1 \boldsymbol{E}_{1b}^{+} = \frac{1}{2}(\boldsymbol{H}_b + \eta_1 \boldsymbol{E}_b)$$
$$\boldsymbol{H}_{1b}^{-} = -\eta_1 \boldsymbol{E}_{1b}^{-} = \frac{1}{2}(\boldsymbol{H}_b - \eta_1 \boldsymbol{E}_b)$$

The fields at boundary a at the same point in time can be determined by applying a phase shift from 0 to –d (where d is the thickness of the thin film). The phase factor for the positive-going wave is exp(i$\delta$) and for the negative-going wave it is exp(-i$\delta$), where

$$\delta = 2\pi n_2 d\cos\vartheta_1/\lambda$$

The values of the electric and magnetic fields at boundary a become:

$$\boldsymbol{E}_{1a}^{+} = \boldsymbol{E}_{1b}^{+} e^{i\delta} = \frac{1}{2}\left(\frac{\boldsymbol{H}_b}{\eta_1} + \boldsymbol{E}_b\right) e^{i\delta}$$
$$\boldsymbol{E}_{1a}^{-} = \boldsymbol{E}_{1b}^{-} e^{-i\delta} = \frac{1}{2}\left(-\frac{\boldsymbol{H}_b}{\eta_1} + \boldsymbol{E}_b\right) e^{-i\delta}$$
$$\boldsymbol{H}_{1a}^{+} = \boldsymbol{H}_{1b}^{+} e^{i\delta} = \frac{1}{2}(\boldsymbol{H}_b + \eta_1 \boldsymbol{E}_b) e^{i\delta}$$
$$\boldsymbol{H}_{1a}^{-} = \boldsymbol{H}_{1b}^{-} e^{-i\delta} = \frac{1}{2}(\boldsymbol{H}_b - \eta_1 \boldsymbol{E}_b) e^{-i\delta}$$

so that

$$\boldsymbol{E}_a = \boldsymbol{E}_{1a}^{+} + \boldsymbol{E}_{1a}^{-} = \boldsymbol{E}_b\left(\frac{e^{i\delta} + e^{-i\delta}}{2}\right) + \boldsymbol{H}_b\left(\frac{e^{i\delta} - e^{-i\delta}}{2\eta_1}\right) = \boldsymbol{E}_b cos\delta + \boldsymbol{H}_b\frac{isin\delta}{\eta_1}$$

$$\boldsymbol{H}_a = \boldsymbol{H}_{1a}^{+} + \boldsymbol{H}_{1a}^{-} = \boldsymbol{E}_b\eta_1\left(\frac{e^{i\delta} - e^{-i\delta}}{2}\right) + \boldsymbol{H}_b\left(\frac{e^{i\delta} + e^{-i\delta}}{2}\right) = \boldsymbol{E}_b i\eta_1 sin\delta + \boldsymbol{H}_b cos\delta$$

This can be written in matrix form as follows:

$$\begin{bmatrix}\mathbf{E}_a\\ \mathbf{H}_a\end{bmatrix} = \begin{bmatrix}\cos\delta & \dfrac{i\sin(\delta)}{\eta_2}\\ i\eta_2\sin\delta & \cos\delta\end{bmatrix}\begin{bmatrix}\mathbf{E}_b\\ \mathbf{H}_b\end{bmatrix}$$